Check for updates

JGR Oceans

RESEARCH ARTICLE
10.1029/2026JC024496

Satellite Observations of Annual Variations in the Ocean-Induced Magnetic Field From the Tropical Oceans

Christopher C. Finlay[1], Clemens Kloss[1], Rasmus M. Blangsbøll[1], Jakub Velímský[2], Veronika Ucekajová[2], and Ondřej Kureš[2]

[1]Division of Geomagnetism and Geospace, DTU Space, Technical University of Denmark, Kongens Lyngby, Denmark, [2]Department of Geophysics, Faculty of Mathematics and Physics, Charles University, Prague, Czech Republic

Key Points:

- An algorithm is presented for estimating the band-limited, ocean circulation induced, magnetic field from satellite observations
- Modest localized agreement is found between simulated and observed magnetic field annual variations in parts of the Indian and Atlantic oceans
- Observed and simulated signals also show similar dynamics (westward and eastward propagation) in these locations

Correspondence to:
C. C. Finlay,
cfinlay@space.dtu.dk

Citation:
Finlay, C. C., Kloss, C., Blangsbøll, R. M., Velímský, J., Ucekajová, V., & Kureš, O. (2026). Satellite observations of annual variations in the ocean-induced magnetic field from the tropical oceans. *Journal of Geophysical Research: Oceans*, *131*, e2026JC024496. https://doi.org/10.1029/2026JC024496

Received 22 APR 2026
Accepted 14 OCT 2026

Author Contributions:
Conceptualization: Christopher C. Finlay, Jakub Velímský
Data curation: Clemens Kloss, Jakub Velímský, Veronika Ucekajová
Formal analysis: Christopher C. Finlay, Clemens Kloss, Jakub Velímský
Funding acquisition: Christopher C. Finlay, Jakub Velímský
Investigation: Christopher C. Finlay, Clemens Kloss, Rasmus M. Blangsbøll, Veronika Ucekajová, Ondřej Kureš
Methodology: Christopher C. Finlay, Clemens Kloss, Jakub Velímský
Project administration: Christopher C. Finlay, Jakub Velímský
Software: Christopher C. Finlay, Clemens Kloss, Rasmus M. Blangsbøll,

© 2026 The Author(s). Journal of Geophysical Research: Oceans published by Wiley Periodicals LLC on behalf of American Geophysical Union.
This is an open access article under the terms of the Creative Commons Attribution License, which permits use, distribution and reproduction in any medium, provided the original work is properly cited.

Abstract The Ocean Induced Magnetic Field (OIMF) is produced by the motion of the electrically conducting ocean through Earth's ambient magnetic field, and its time-dependence carries information concerning ocean dynamics and electrical conductivity changes. Here, we present an algorithm to estimate, from satellite magnetic field observations, the band-limited OIMF, focusing on annual variations (periods 300–430 days) and spherical harmonic degrees 19 to 28. We work with Along-Track and East-West differences of the vector magnetic field and intensity measured by the *Swarm* satellite constellation. After applying corrections for known non-oceanic signals, we construct a time-dependent internal field model which is subsequently filtered in space and time to provide an estimate of the OIMF. We assess this estimate via comparisons to a simulated OIMF computed from the Copernicus CMEMS mean ocean model that is based on assimilated oceanographic observations. Focusing on the tropics during the solar minimum years 2018.5–2020.5, we find modest but encouraging localized agreement between the estimated and simulated OIMF in the Indian Ocean (correlation coefficient of 0.3 for spatial structures, up to 0.8 in time-longitude plots). The agreement is in terms of spatial-temporal structures rather than amplitude. In other ocean basins, where the OIMF in the studied spatio-temporal band is weaker, we find less agreement, with the exception of some parts of the central Pacific and the western North Atlantic. Our results suggest it is possible to retrieve the general circulation OIMF from satellite magnetic field measurements, in regions where the ocean-induced signal is strong, provided sufficient, high quality, geomagnetically-quiet, satellite data are available.

Plain Language Summary The oceans are a key component of our natural environment. Improved monitoring of the movements, temperature and salinity, throughout the volume of the oceans, is needed to advance our understanding of the Earth system. Here, we study small magnetic fields that are generated when the ocean moves across Earth's magnetic field. These are sensitive to the motions of the ocean and to its electrical conductivity which depends on its temperature and salinity. If such magnetic signals can be detected by satellites they can provide additional information on the state and dynamics of the oceans. We describe here a method for studying the magnetic signal produced by the ocean general circulation in satellite data, focusing on variations with period around 1 year and wavelengths of 1,400–2,100 km, and using data collected by ESA's *Swarm* satellite trio. The signal we identify shows encouraging localized agreement with the expected ocean-generated magnetic signal in the Indian ocean, and in some parts of the western north Atlantic and central Pacific oceans, rather than a general agreement across the tropics. Improved performance should be possible in the future when satellite data are collected closer to Earth's surface and when more frequent repeated measurements are available.

1. Introduction

The general circulation of the ocean, its dynamics, and related changes in temperature and salinity are of central importance in efforts to better understand Earth's climate system (Siedler et al., 2013; Williams & Follows, 2011). Much has been learned from in situ measurements such as depth profiles, moored and drifting buoys, measurements made by floats, and by remote sensing of the sea surface height, temperature, and salinity by satellites. Spatial sampling of the properties of interest over the entire volume of the ocean nevertheless remains sparse. Complementary observations, providing independent constraints on integrated ocean properties, are therefore of considerable interest.

It has been recognized since Faraday's early investigations of electromagnetic induction (Faraday, 1832) that motion of water through Earth's magnetic field will result in induced electrical currents and associated

21699291, 2026, 11, Downloaded from https://agupubs.onlinelibrary.wiley.com/doi/10.1029/2026JC024496 by Christopher Finlay - Danish Technical Knowledge , Wiley Online Library on [12/11/2026]. See the Terms and Conditions (https://onlinelibrary.wiley.com/terms-and-conditions) on Wiley Online Library for rules of use; OA articles are governed by the applicable Creative Commons License

Jakub Velímský, Veronika Ucekajová, Ondřej Kureš
Supervision: Jakub Velímský
Validation: Christopher C. Finlay, Rasmus M. Blangsbøll, Jakub Velímský, Veronika Ucekajová
Visualization: Christopher C. Finlay, Clemens Kloss, Rasmus M. Blangsbøll, Veronika Ucekajová, Ondřej Kureš
Writing – original draft: Christopher C. Finlay
Writing – review & editing: Christopher C. Finlay, Clemens Kloss, Rasmus M. Blangsbøll, Jakub Velímský

motionally-induced magnetic fields. Thanks to advances in geomagnetic field measurements techniques, and theoretical understanding, by the mid twentieth century it became possible to detect such ocean-induced magnetic field (OIMF) signals and interpret the signals in terms of the motions of the ocean and their electrical conductivity (Larsen, 1968; Longuet-Higgins, 1949; Sanford, 1971).

Starting from the 1990s increasingly sophisticated numerical simulations of the OIMF have been carried out. The pioneering study of Stephenson and Bryan (1992) established the basic expected global structure and amplitude of the OIMF due to the general circulation of the ocean, with the time-averaged OIMF dominated by induction due to the Antarctic Circumpolar Current and amplitudes of order 2 nT predicted at Earth's surface. Stephenson and Bryan also set out the basic structure expected for OIMF annual variations, related for example, to seasonal variations in ocean flows, finding this to be most prominent in the tropics, particularly in the Indian Ocean. Tyler et al. (1997) independently arrived at broadly similar results for the global OIMF but pointed out uncertainties related to the distribution of electrical conductivity below the oceans. Manoj et al. (2006) later considered improved ocean flow models, included in their model sediment conductances and an underlying 1D mantle conductivity, and focused on the expected OIMF at satellite altitude. Considering summer-winter differences Manoj et al. reiterated the interest of the Indian Ocean as a region of strong OIMF variability (amplitude of order 0.2 nT at satellite altitude) which they attributed to processes related to South Asian monsoon. Irrgang et al. (2018) found in their simulations that the general circulation OIMF is caused primarily by ocean currents in the top 2000 m, with annual variations affected by sub-surface currents as deep as 1,000 m. Velímský et al. (2019) highlighted the importance of galvanic coupling at the ocean floor and illustrated in their simulations how strong toroidal magnetic fields, generated within the ocean by motional induction, can, in the presence of horizontal gradients in electrical conductivity, make an important contribution to the poloidal OIMF observed at satellite altitude.

An important inter-comparison of OIMF simulation codes was carried out by Šachl et al. (2019). They recommended galvanic coupling should be included when making comparisons with satellite magnetic measurements, finding that annual variations remained present at low spherical harmonic degree even when such coupling was included. In a precursor to the present work, Finlay et al. (2024) compared simulated OIMFs to magnetic signals expected from other geophysical sources. They argued that OIMF annual variations should be accessible in satellite magnetic field data at spherical harmonic degree above 16, where signals from Earth's core are strongly attenuated and there is somewhat less impact expected from ionospheric and magnetospheric sources. This supported an earlier idea that there may be a spectral window where ocean-induced fields are more easily accessible (Tyler & Mysak, 1995). Taken together, the past three decades of work on simulating the OIMF, lead us to expect that although the signal at satellite altitude is small, its annual variations (amplitude of order 0.2 nT) are potentially observable at spherical harmonic degrees above 16, and that such signals will contain information on sub-surface ocean flow dynamics and electrical conductivity variations.

Progress has also been made in recent years on retrieving the OIMF from satellite observations, although the focus has primarily been on signals produced by ocean tides, which are easier to extract thanks to their precisely known periods. Tyler et al. (2003) were the first to identify the OIMF signal of the diurnal M_2 tide in magnetic measurements from the CHAMP satellite. Sabaka et al. (2015) later co-estimated tidal signals along with those of other sources, also using CHAMP data, while Sabaka et al. (2016) used a similar technique but took advantage of magnetic field gradients collected by ESA's *Swarm* satellites. Finite-difference observations (usually referred to as field gradients) are useful for minimizing the impact of imperfectly modeled large-scale magnetospheric signals that otherwise limit the fidelity of the OIMF recovery. Grayver and Olsen (2019) and more recently Grayver et al. (2024) have succeeded in extracting the weaker signatures of other tidal constituents including N_2, O_1 and Q_1, utilizing strict geomagnetic quiet-time data selection criteria and field gradients from the CHAMP and *Swarm* satellites, and validating their retrievals by comparisons to simulated OIMF tidal signals. Tidal magnetic signals have also been studied using a Kalman filter based inversion method by Saynisch-Wagner et al. (2021) and linked to ocean tidal transports by Saynisch-Wagner et al. (2023). By such methods it has been shown to be possible to retrieve OIMF signals as small as 0.1 nT from *Swarm* satellite data (Grayver et al., 2024).

Regarding the general circulation OIMF and its variations, there have so far been comparatively few observational studies. Golubev (2012) have presented magnetic anomalies in the Southern ocean based on CHAMP satellite data that they argued were due to the OIMF general circulation signal. More recently, Hornschild et al. (2022) proposed a method for extracting the general circulation OIMF, by imposing an a-priori temporal

21699291, 2026, 11, Downloaded from https://agupubs.onlinelibrary.wiley.com/doi/10.1029/2026JC024496 by Christopher Finlay - Danish Technical Knowledge , Wiley Online Library on [12/11/2026]. See the Terms and Conditions (https://onlinelibrary.wiley.com/terms-and-conditions) on Wiley Online Library for rules of use; OA articles are governed by the applicable Creative Commons License

behavior and determining local scale factors to retrieve the spatial structure within a Kalman filter framework, demonstrating the feasibility of this approach in experiments with simulated observations. With regard to ground-based magnetic field observations, Winch and Runcorn (1993) had earlier directed attention to annual field variations, arguing that part of this was of internal origin and strongest over the oceans, so possibly related to annual variations in the ocean circulation. The link to motional induction in the ocean was however unclear and the sparsity of ground observatory data in oceanic regions made detailed comparisons problematic. It therefore remains to be demonstrated that the general circulation OIMF can be reliably extracted from geomagnetic observations.

Here, we present a scheme for estimating the general circulation OIMF in a chosen spatio-temporal band. We focus on wavelengths of 1,400–2100 km corresponding to spherical harmonic degrees 19 to 28, and on the annual period band of 300–430 days. We expect the OIMF signal in this spatio-temporal band to be significant compared with that from other geomagnetic field sources. Building on successes in using satellite-measured field gradients to study the lithospheric magnetic field at such spatial wavelengths (Olsen et al., 2017) we follow a sequential data processing scheme using Along-Track and East-West gradient data from the three *Swarm* satellites, solving for a time-dependent internal field model and subsequently, as a post-processing step, filtering in space and time. In an effort to avoid as far as possible the impacts of unmodelled ionospheric and magnetospheric fields (and their induced counterparts) we focus on the solar minimum interval of 2018.5–2020.5. During this time we find it is possible to retrieve the targeted band-limited OIMF signal in regions where the expected signal is large, such as the Indian Ocean.

In Section 2 we describe the satellite magnetic field observations from the *Swarm* mission that are the basis of this study and explain the criteria used to select data that are most useful for extracting the OIMF signal. In Section 3 we describe our scheme for estimating the band-limited OIMF signal from satellite data, including the corrections applied to the data, time-dependent geomagnetic field modeling, and post-processing (i.e., spatio-temporal filtering). We present our results in Section 4, comparing the estimated OIMF to predictions from advanced OIMF simulations based on oceanographic data. Results are discussed separately for the Indian, Pacific and Atlantic basins considering both single epoch snapshots and time-longitude plots of the radial field at Earth's surface. In Section 5 we discuss what has been learned, the limitations of the present study, and prospects for future improvements. Conclusions are offered in Section 6 and Appendix A presents tests of the method on synthetic data.

2. Satellite Observations

2.1. The *Swarm* Satellite Mission

In this study we exclusively use data collected by the *Swarm* satellite trio (Friis-Christensen et al., 2006), that has been providing high-accuracy vector measurements of Earth's magnetic field since November 2013 (Olsen & Floberghagen, 2018). We considered a 10 year interval of data from the *Swarm* satellites from 25th November 2013 to 25th November 2023, encompassing geomagnetically quiet solar minimum conditions from mid 2018 to mid 2020. We worked with the most up-to-date operational *Swarm* L1b 1 Hz magnetic field daily Common Data Format data files, as available in February 2025, which were primarily data versions 0605/0606/0607.

2.2. Data Selection

The 1 Hz *Swarm* Mag-L data product was sub-sampled to 15 s values; this made the amount of data more manageable whilst still adequately capturing magnetic field variations on the length and time-scales of interest. Data from geomagnetically disturbed times were removed. Disturbed times were identified based on threshold values for (i) the *Kp* geomagnetic activity range index (Matzka et al., 2021) (ii) the magnitude of the hourly rate of change of the *RC*-index, which tracks the amplitude of the symmetric part of the magnetospheric ring current (Olsen et al., 2014), (iii) the interplanetary magnetic field (IMF) B_z component in Geocentric Solar Magnetospheric coordinates and (iv) the empirical solar wind-magnetosphere coupling parameter ϵ (Kloss et al., 2026; Newell et al., 2007), derived from observations of the IMF and the solar wind speed, here based on inputs averaged over a 2-hr rolling window. The implemented threshold values are collected in Table 1. Suspected erroneous data were also removed based on the recommended quality flags (Flags_B and Flags_q) provided in the

21699291, 2026, 11, Downloaded from https://agupubs.onlinelibrary.wiley.com/doi/10.1029/2026JC024496 by Christopher Finlay - Danish Technical Knowledge , Wiley Online Library on [12/11/2026]. See the Terms and Conditions (https://onlinelibrary.wiley.com/terms-and-conditions) on Wiley Online Library for rules of use; OA articles are governed by the applicable Creative Commons License

Table 1
Summary of the Geomagnetic Selection Criteria Applied to the Satellite Data

Variable	Criterion
Kp	$<2^o$
$\lvert\frac{dRC}{dt}\rvert$	<2 nT h^{-1}
IMF B_z	>0 nT
ϵ	<2.4 mVm^{-1}
Flags_B	not equal to 255
Flags_q	not equal to 255
$\lvert\Delta B_r\rvert$, $\lvert\Delta B_\theta\rvert$, $\lvert\Delta B_\phi\rvert$	$<1{,}000$ nT
ζ_s, non-polar regions	$>100°$
LT, polar regions	20:00 to 04:00

Note. Data points were selected only if all criteria were satisfied at the time of observation.

Swarm magnetic field product data files. Remaining large outliers were removed based on component-wise thresholds (see Table 1) on differences ΔB_r, ΔB_θ, ΔB_ϕ with respect to the CHAOS-7.17 field model (Finlay et al., 2020).

In non-polar regions (defined as regions with absolute Quasi-dipole latitudes less than or equal to 55°, see Laundal and Richmond (2017) for the definition of Quasi-dipole latitude) only data from dark regions, defined as when the solar zenith angle $\zeta_s > 100°$, were used. In the polar regions (absolute Quasi-dipole latitudes above 55°), in order to retain some data during polar summer, no selection criteria based on ζ_s was implemented, instead local times were restricted to be from the night-side between 20:00 and 04:00. A summary of all the implemented data selection criteria is given in Table 1.

Both vector and scalar intensity magnetic field measurements were used at non-polar latitudes, while in the polar region only scalar intensity data was used, in an effort to avoid contamination from field-aligned current signatures that are prominent in the horizontal field components. Rather than working with the vector and scalar magnetic field data directly we instead considered Along-Track and East-West finite differences (i.e., approximate gradients) of the measurements. These differences are less affected by large-scale correlated noise, are highly sensitive to small scales in the internal field (Olsen et al., 2017), and synthetic tests showed the OIMF signal could be well recovered using field differences alone (see Appendix A). We follow Olsen et al. (2015) and compute Along-Track differences using measurement pairs from each satellite separated in time by 15 s. East-West differences were computed from pairs of measurements made by *Swarm* A and C, with the *Swarm* C 1 Hz data selected that was closest in latitude to a selected *Swarm* A datum, within a 100 s time window. The temporal distribution of the resulting vector and scalar field gradients that comprise our data set are presented in Figure 1. Note that more data satisfied the selection criteria during the solar minimum period, 2018.5 to 2020.5. For the vector field data and their differences we worked with the field components in spherical polar co-ordinates (B_r, B_θ, B_ϕ), following a rotation from the instrument frame, based on the measured attitudes and in-flight Euler-angles estimated in the CHAOS-7.17 field model. Initially, for simplicity, isotropic data errors of 0.2 nT were allocated for all field differences, both scalar and vector. However since long-tailed error distributions were accounted for by use of Huber-weights during the field model estimation, the data were iteratively re-weighted during the estimation procedure, further details are given in Section 3.3.

3. Methodology

3.1. Overview of OIMF Estimation Algorithm

A summary of the scheme we used to extract the band-limited OIMF signal from *Swarm* satellite magnetic field measurements is given in Algorithm 1. Six main steps are involved: (1) Selection of data based on criteria to minimize signals from magnetospheric and ionospheric sources, as described in Section 2.2, (2) Data corrections for known non-OIMF fields, (3) Use of field differences, (4) Estimation of a time-dependent internal field model

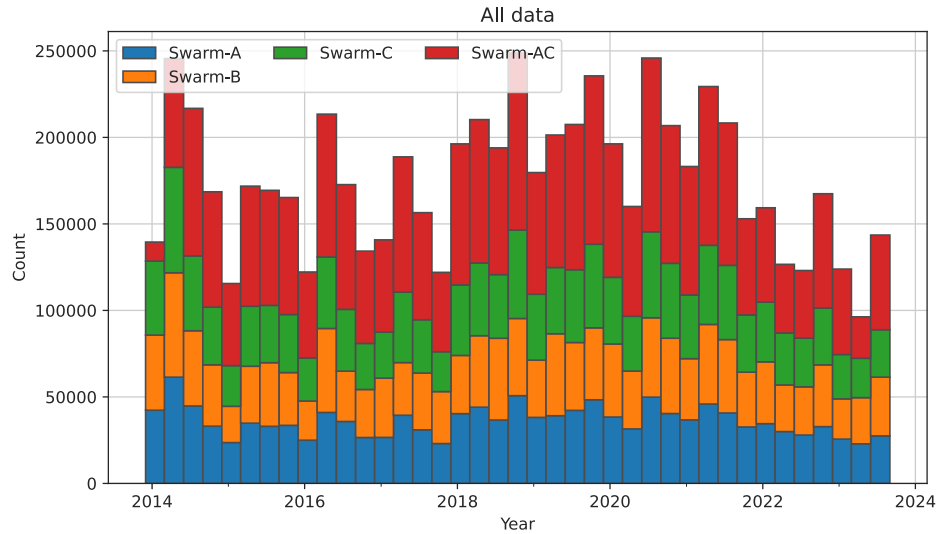


Figure 1. Total number of selected field difference data, both vector and scalar, versus time, considering 3-month bins. The variations shown here are a result of the implemented data selection criteria (primarily the geomagnetic quiet-time criteria).

from the field differences, (5) Post-processing to focus on a specified spatio-temporal band, (6) Evaluation of the radial magnetic field from the resulting filtered field model on a regular grid at Earth's surface. Steps (2)–(6) are described in more detail below.

Algorithm 1: Estimation of band-limited ocean-induced magnetic field.

input: Satellite magnetic field data set for example, SW_OPER_MAGX_LR_1B
Field models for corrections: CHAOS, LCS-1, AMPS and CI
Spherical harmonic truncation levels: N_{td}, N_{int}
Regularization matrices $\underline{\underline{\Lambda}}_0$, $\underline{\underline{\Lambda}}_2$, $\underline{\underline{\Lambda}}_3$ and hyperparameters $\lambda_0, \lambda_2, \lambda_3$

output: Estimated ocean-induced magnetic field $\widehat{\mathbf{B}}_{oi}$, gridded at Earth's surface

(1) **Data selection:**
Geomagnetic quiet times, non-polar dark, polar night-side, remove suspect data based on flags and outlier thresholds (Table 1). Resulting dataset is $\mathbf{B}^{\text{Obs}}$

(2) **Data corrections: Equations 1–3**

$$\mathbf{B}^{\text{Obs,corr}} = \mathbf{B}^{\text{Obs}} - (\mathbf{B}^{\text{Ext,corr}} + \mathbf{B}^{\text{Int,corr}})$$

$$\mathbf{B}^{\text{Int,corr}} = \mathbf{B}^{\text{CHAOS,core}} + \mathbf{B}^{\text{LCS1,crust}}$$

$$\mathbf{B}^{\text{Ext,corr}} = (1 - w)(\hat{\alpha}\mathbf{B}^{\text{Ion,AMPS}} + \mathbf{B}^{\text{Mag,CHAOS}}) + w\left(\hat{\beta}\mathbf{B}^{\text{Ion,CI}} + \mathbf{B}^{\text{Mag,CI}} + \mathbf{B}_{\text{off}}\right)$$

(3) **Use field finite differences:**
$\Delta\mathbf{B}^{\text{Obs,corr}}$ where Δ denotes Along-Track or East-West data field differences.
Vector differences $|\lambda_{QD}| \leq 55°$. Scalar anomaly differences at all latitudes.

(4) **Estimate time-dependent internal field model: Equations 12–20** $\mathbf{B} = -\nabla V$

$$V^{\text{int}}(r, \vartheta, \varphi, t) = a \sum_{n=1}^{N_{\text{int}}} \sum_{m=0}^{n} \left(\frac{a}{r}\right)^{n+1} \left[g_n^m(t)\cos m\varphi + h_n^m(t)\sin m\varphi\right] P_n^m(\cos\vartheta)$$

Time-dependent up to SH degree $N_{td} = 30$, static at higher degree up to $N_{int} = 50$.
Estimate model coefficients $\mathbf{m}$ by iteratively minimizing

$$\mathcal{J} = \mathbf{e}^{\text{T}}\underline{\underline{\mathbf{W}}}\mathbf{e} + \lambda_0\mathbf{m}^{\text{T}}\underline{\underline{\Lambda}}_0\mathbf{m} + \lambda_2\mathbf{m}^{\text{T}}\underline{\underline{\Lambda}}_2\mathbf{m} + \lambda_3\mathbf{m}^{\text{T}}\underline{\underline{\Lambda}}_3\mathbf{m} \quad \text{with} \quad \mathbf{e} = \left(\Delta\mathbf{B}^{\text{Obs,corr}} - \Delta\mathbf{B}\right)$$

$\widehat{\mathbf{B}}$ is the modeled field, from the model $\widehat{\mathbf{m}}$, obtained after convergence.

(5) **Filter in spherical harmonic and time domains:**
Retain only SH degrees: $19 \leq n \leq 28$
Retain only SH orders: $6 \leq m \leq n - 1$
4th order Butterworth Bandpass temporal filter: 300 days $\leq T_{pass} \leq$ 430 days

21699291, 2026, 11, Downloaded from https://agupubs.onlinelibrary.wiley.com/doi/10.1029/2026JC024496 by Christopher Finlay - Danish Technical Knowledge , Wiley Online Library on [12/11/2026]. See the Terms and Conditions (https://onlinelibrary.wiley.com/terms-and-conditions) on Wiley Online Library for rules of use; OA articles are governed by the applicable Creative Commons License

Such that $\hat{\mathbf{B}} \rightarrow \hat{\mathbf{B}}_{oi}$

(6) **Grid radial field at Earth's surface:**

Evaluate $\hat{\mathbf{B}}_{oi}$ at $r = a$

Restrict grid to latitudes below $\pm 30°$ and mask continental regions if desired.

3.2. Data Corrections

In order to focus as much as possible on the OIMF signal, estimates of well characterized non-oceanic fields were first removed from the *Swarm* satellite data. The applied corrections were of the form

$$\mathbf{B}^{\text{Obs,corr}} = \mathbf{B}^{\text{Obs}} - \left(\mathbf{B}^{\text{Ext,corr}} + \mathbf{B}^{\text{Int,corr}}\right), \tag{1}$$

where $\mathbf{B}^{\text{Obs}}$ are the uncorrected observed magnetic field data collected by the *Swarm* satellites, $\mathbf{B}^{\text{Obs,corr}}$ are the data after corrections have been applied. The corrections applied for known internal fields were

$$\mathbf{B}^{\text{Int,corr}} = \mathbf{B}^{\text{CHAOS}} + \mathbf{B}^{\text{LCS1}} \tag{2}$$

where $\mathbf{B}^{\text{CHAOS}}$ are the corrections for large-scale internal sources in the Earth's core and crust, taken from the CHAOS-7.17 field model, see Finlay et al. (2020), up to spherical harmonic degree 25, and $\mathbf{B}^{\text{LCS1}}$ are corrections for the smaller-scale crustal field, taken from the LCS-1 model (Olsen et al., 2017) from spherical harmonic degree 26 to 120. The vector field corrections were calculated from the field models at the locations of the satellite data.

The corrections applied for fields due to external sources were based on a combination of the CHAOS and AMPS models (Finlay et al., 2020; Laundal et al., 2018) in polar regions and the CI model (Sabaka et al., 2018) in non-polar regions. Both models provide global spherical harmonic representations of the ionospheric field, but the AMPS model is better for describing the polar current systems, driven by the magnetosphere-solar wind interaction, whereas the CI ionospheric field is better for the non-polar current systems, produced by the ionospheric wind dynamo (Yamazaki & Maute, 2016). Since the AMPS model lacks a description of the magnetospheric field, we combined it with the CHAOS magnetospheric field in the polar regions. In detail, the external field corrections were of the form

$$\mathbf{B}^{\text{Ext,corr}} = (1-w)\left(\hat{\alpha}\mathbf{B}^{\text{Ion–AMPS}} + \mathbf{B}^{\text{Mag–CHAOS}}\right) + w\left(\hat{\beta}\mathbf{B}^{\text{Ion–CI}} + \mathbf{B}^{\text{Mag–CI}} + \mathbf{B}_{\text{off}}\right), \tag{3}$$

where $\mathbf{B}^{\text{Ion}-\text{AMPS}}$ is the ionospheric field predicted by the AMPS model, $\mathbf{B}^{\text{Mag}-\text{CHAOS}}$ is the magnetospheric field from the CHAOS model and $\mathbf{B}^{\text{Ion}-\text{CI}}$, $\mathbf{B}^{\text{Mag}-\text{CI}}$ are the ionospheric and magnetospheric fields from the CI model. $\mathbf{B}_{\text{off}} = \mathbf{B}^{\text{Int}-\text{CI}} - \mathbf{B}^{\text{Int}-\text{CHAOS}}$ is the difference between the CI and CHAOS internal field models, which we found must be included to avoid offsets between the CI and CHAOS ionospheric fields, w is a window function providing a smooth transition between the QD polar latitude region (where AMPS ionospheric field plus CHAOS magnetospheric field is favored as it is expected to perform best) and non-polar QD latitude regions (where the CI model is favored), defined as

$$w(\lambda_{\text{QD}}) = \begin{cases} 1, & |\lambda_{\text{QD}}| < \lambda_{\min} \\ \frac{1}{2}\left[1 + \cos\left(\pi \frac{|\lambda_{\text{QD}}| - \lambda_{\min}}{\lambda_{\max} - \lambda_{\min}}\right)\right], & \lambda_{\min} \le |\lambda_{\text{QD}}| < \lambda_{\max} \\ 0, & |\lambda_{\text{QD}}| \ge \lambda_{\max} \end{cases} \tag{4}$$

with $\lambda_{\min} = 45°$ and $\lambda_{\max} = 65°$.

21699291, 2026, 11, Downloaded from https://agupubs.onlinelibrary.wiley.com/doi/10.1029/2026JC024496 by Christopher Finlay - Danish Technical Knowledge , Wiley Online Library on [12/11/2026]. See the Terms and Conditions (https://onlinelibrary.wiley.com/terms-and-conditions) on Wiley Online Library for rules of use; OA articles are governed by the applicable Creative Commons License

$\hat{\alpha}$ and $\hat{\beta}$ are daily rescaling factors estimated for the ionospheric fields, motivated by the known lack of day-to-day variability in the AMPS and CI climatological ionospheric field models. These rescaling factors were determined by daily robust least-square fits using Huber weights (Huber, 2004) according to

$$\hat{\alpha} = \underset{\alpha}{\operatorname{argmin}} ||\mathbf{B}^{\text{Res–CHAOS}} - \alpha \mathbf{B}^{\text{Ion–AMPS}}||^2, \tag{5}$$

and

$$\hat{\beta} = \underset{\beta}{\operatorname{argmin}} ||\mathbf{B}^{\text{Res–CI}} - \beta \mathbf{B}^{\text{Ion–CI}}||^2 \tag{6}$$

where

$$\mathbf{B}^{\text{Res–CHAOS}} = \mathbf{B}^{\text{Obs}} - \mathbf{B}^{\text{Int–CHAOS}} - \mathbf{B}^{\text{Mag–CHAOS}}. \tag{7}$$

and

$$\mathbf{B}^{\text{Res–CI}} = \mathbf{B}^{\text{Obs}} - \mathbf{B}^{\text{Int–CI}} - \mathbf{B}^{\text{Mag–CI}}. \tag{8}$$

Only data from QD polar regions ($|\lambda_{\text{QD}}| > 45°$) were used to estimate $\hat{\alpha}$, while only data from QD non-polar latitudes ($|\lambda_{\text{QD}}| \leq 65°$) were used to estimate $\hat{\beta}$, allowing for an overlap in QD latitude. At mid-latitudes this rescaling decreased the daily RMS of the corrected radial field by an average of 0.3 nT (15%). Although the decrease is relatively small and is limited to the radial component, it suggests that our scheme provides a useful reduction of external field contamination at these latitudes.

3.3. Global Modeling of Time-Dependent Internal Field

3.3.1. Forward Modeling Scheme

The vector magnetic field modeled here is an anomaly field

$$\mathbf{B} = \mathbf{B}_{\text{tot}} - \mathbf{B}_0 \tag{9}$$

where $\mathbf{B}_{\text{tot}}$ denotes the total magnetic field, including all sources, and $\mathbf{B}_0$ is a known background field that is removed prior to modeling

$$\mathbf{B}_0 = \mathbf{B}^{\text{Ext,corr}} + \mathbf{B}^{\text{Int,corr}} \tag{10}$$

where, as in Section 3.2, $\mathbf{B}^{\text{Int,corr}}$ denotes pre-estimated core and crustal fields and $\mathbf{B}^{\text{Ext,corr}}$ denotes pre-estimated fields from ionospheric and magnetospheric sources. $\mathbf{B}$ thus contains the OIMF of interest, along with contributions from other unmodelled or imperfectly corrected sources.

Since $|\mathbf{B}| \ll F_0 = |\mathbf{B}_0|$ we are also able to define and work with a scalar anomaly field

$$F = F_{\text{tot}} - F_0 \approx \frac{\mathbf{B} \cdot \mathbf{B}_0}{|\mathbf{B}_0|}. \tag{11}$$

When calculating the scalar anomaly field we considered only the internal field in F_0 and $\mathbf{B}_0$; tests showed this had little impact on the modeled field at degrees above 18 that are the focus here. The anomaly field in the region of interest, between satellite altitude, where magnetic measurements are collected, and the Earth's surface where we wish to evaluate it, is modeled as a potential field. This is reasonable when time-changes in the magnetic field are sufficiently slow (periods longer than approximately 1s, well satisfied here), and provided that the current density in the region under consideration can be neglected. We therefore can write the anomaly field $\mathbf{B}$ as the gradient of a scalar magnetic potential V

21699291, 2026, 11, Downloaded from https://agupubs.onlinelibrary.wiley.com/doi/10.1029/2026JC024496 by Christopher Finlay - Danish Technical Knowledge , Wiley Online Library on [12/11/2026]. See the Terms and Conditions (https://onlinelibrary.wiley.com/terms-and-conditions) on Wiley Online Library for rules of use; OA articles are governed by the applicable Creative Commons License

$$\mathbf{B} = -\nabla V. \tag{12}$$

Since magnetic fields are divergence free, V satisfies Laplace's equation. The general solution to Laplace's equation involves contributions from both internal and external sources

$$V = V^{\text{int}} + V^{\text{ext}}. \tag{13}$$

Here, we assume that the external sources have already been modeled and removed and consider only the potential due to internal sources, which is described by the series expansion

$$V^{\text{int}}(r,\vartheta,\phi,t) = a\sum_{n=1}^{N_{\text{int}}}\sum_{m=0}^{n}\left(\frac{a}{r}\right)^{n+1}\left[g_n^m(t)\cos m\phi + h_n^m(t)\sin m\phi\right]P_n^m(\cos\vartheta), \tag{14}$$

where $a = 6371.2\,\text{km}$ is a reference radius, chosen to be Earth's mean spherical radius, (r,ϑ,ϕ) are the geographic coordinates, t is time, P_n^m are Schmidt quasi-normalized associated Legendre functions of degree n and order m, and $\{g_n^m, h_n^m\}$ are known in geomagnetism as the Gauss coefficients. Up to spherical harmonic degree $N_{\text{td}} = 30$ time-dependence of the Gauss coefficients is considered, parameterized using an expansion in sixth order B-splines,

$$g_n^m(t) = \sum_k g_{n,k}^m B_k(t), \tag{15}$$

where the index k runs over the spline basis functions which are chosen to have a spline knot separation of 60 days. This resulted in 60,480 model parameters associated with the time-dependent internal field, which is considerably more than one typically estimates for a core field model. Field variations in the estimated model showed little power at periods shorter than 90 days due to the applied temporal regularization, see Section 3.3.2. The maximum spherical harmonic degree for the entire expansion is $N_{\text{int}} = 50$; the modeled field for degrees 31 to 50 is static.

3.3.2. Field Model Estimation

The model parameters specifying the internal field are collected into a vector $\mathbf{m}$ and estimated from the *Swarm* satellite magnetic field observations using a regularized, robust, least-squares approach. This involves iteratively minimizing the cost function

$$\mathcal{J} = \mathbf{e}^{\text{T}}\underline{\underline{\mathbf{W}}}\mathbf{e} + \lambda_0\mathbf{m}^{\text{T}}\underline{\underline{\Lambda}}_0\mathbf{m} + \lambda_2\mathbf{m}^{\text{T}}\underline{\underline{\Lambda}}_2\mathbf{m} + \lambda_3\mathbf{m}^{\text{T}}\underline{\underline{\Lambda}}_3\mathbf{m}, \tag{16}$$

where the first term is a robust measure of the data misfit, with $\mathbf{e} = \left(\Delta\mathbf{B}^{\text{Obs,corr}} - \Delta\mathbf{B}\right) = \left(\Delta\mathbf{B}^{\text{Obs,corr}} - \mathbf{Gm}\right)$ being a vector of the observed anomaly field differences minus the associated predictions of the anomaly field model $\Delta\mathbf{B} = \mathbf{Gm}$, where $\mathbf{G}$ is the forward model design matrix linking Along-Track and East-West differences of the vector and scalar anomaly fields to the model parameters. $\underline{\underline{\mathbf{W}}} = \underline{\underline{\mathbf{C}}}^{-1/2}\underline{\underline{\mathbf{H}}}\,\underline{\underline{\mathbf{C}}}^{-1/2}$ is a data weight matrix derived from square root factors of the inverse data error covariance matrix, $\underline{\underline{\mathbf{C}}}^{-1/2}$, and $\underline{\underline{\mathbf{H}}}$ is a diagonal matrix of robust data weights, calculated from the residuals at the previous iteration based on a Huber distribution (Constable, 1988; Huber, 2004) relevant for a long-tailed distribution of residuals, and also including a factor $\sin\theta$ that accounts for the data density on polar orbits.

The three final terms in Equation 16 implement respectively spatial regularization, model endpoint temporal regularization, and temporal regularization throughout the model timespan, based on the following quadratic norms

$$\mathbf{m}^{\text{T}}\underline{\underline{\Lambda}}_0\mathbf{m} = \int B_r^2\, d\Omega_a\, dt, \tag{17}$$

21699291, 2026, 11, Downloaded from https://agupubs.onlinelibrary.wiley.com/doi/10.1029/2026JC024496 by Christopher Finlay - Danish Technical Knowledge , Wiley Online Library on [12/11/2026]. See the Terms and Conditions (https://onlinelibrary.wiley.com/terms-and-conditions) on Wiley Online Library for rules of use; OA articles are governed by the applicable Creative Commons License

$$\mathbf{m}^{\mathrm{T}}\underline{\underline{\Lambda}}_2\mathbf{m} = \int \left(\frac{\partial^2 B_r}{\partial t^2}\right)^2 d\Omega_a \Bigg|_{t=t_{\mathrm{start}}} + \int \left(\frac{\partial^2 B_r}{\partial t^2}\right)^2 d\Omega_a \Bigg|_{t=t_{\mathrm{end}}} \tag{18}$$

and

$$\mathbf{m}^{\mathrm{T}}\underline{\underline{\Lambda}}_3\mathbf{m} = \int \left(\frac{\partial^3 B_r}{\partial t^3}\right)^2 d\Omega_a \, dt, \tag{19}$$

where Ω_a is the Earth's surface (radius $r = a$), the integration over time, in the first and third norms, is over the entire timespan of the model, and t_{start} and t_{end} in the second norm are the start and end times of the model. λ_0, λ_2 and λ_3 are hyper-parameters determining the weight given to the three regularization norms. Evaluation of these norms at Earth's surface is appropriate for stabilizing the OIMF, since this originates close to Earth's surface. Note that this is a significant difference compared with the radius used for regularization in most time-dependent internal field models, which is the core-mantle boundary radius since they are focused on modeling the core field (Finlay et al., 2020; Sabaka et al., 2020). In the model presented below we choose $\lambda_0 = 5 \times 10^5 (\mathrm{nT})^{-2}$ and $\lambda_3 = 50\left(\mathrm{nT/yr}^3\right)^{-2}$, in order to give appropriate levels for, respectively, the spatial power spectra of the field and its annual variations, based on levels suggested by OIMF numerical simulations (see Figure 3). We set $\lambda_2 = 500$ $\left(\mathrm{nT/yr}^2\right)^{-2}$ in order to control the field acceleration at the model endpoints.

The cost function in Equation 16 is iteratively minimized using a quasi-Newton method (Tarantola, 2005) with iterations of the form

$$\begin{aligned} \mathbf{m}_{i+1} &= \mathbf{m}_i + \delta\mathbf{m}_i \\ \text{where} \quad \delta\mathbf{m}_i &= \left[\underline{\underline{\mathbf{G}}}^{\mathrm{T}}\underline{\underline{\mathbf{W}}}\,\underline{\underline{\mathbf{G}}} + \lambda_0\underline{\underline{\Lambda}}_0 + \lambda_2\underline{\underline{\Lambda}}_2 + \lambda_3\underline{\underline{\Lambda}}_3\right]^{-1} \\ &\quad \cdot \left[\underline{\underline{\mathbf{G}}}^{\mathrm{T}}\underline{\underline{\mathbf{W}}}\left(\Delta\mathbf{B}^{\mathrm{Obs,corr}} - \mathbf{G}\mathbf{m}_i\right) - \lambda_0\underline{\underline{\Lambda}}_0\mathbf{m}_i - \lambda_2\underline{\underline{\Lambda}}_2\mathbf{m}_i - \lambda_3\underline{\underline{\Lambda}}_3\mathbf{m}_i\right], \end{aligned} \tag{20}$$

where i indicates the previous iteration and $i + 1$ the next. Note that since we are working with vector and scalar anomaly data the forward problem is linear; nonlinearity and the need to iterate comes from the use of Huber weights. In the first iteration the Huber weights are initialized to values 1.0 and 12 iterations were carried out; at the final iteration the maximum fractional change in any model parameter compared with the previous iteration was 1.9×10^{-4}.

3.4. Post-Processing and Applied Filters

Internal field modeling of the *Swarm* satellite observations, as described above, is on its own not sufficient to isolate the OIMF field, due to remaining uncorrected (internal) signals in the data that can be fit by the time-dependent part of our model with spherical harmonics up to degree 30 and a spline knot spacing of 60 days. Post-processing is therefore required to remove parts of the model where we found clear evidence of leakage; we implement this by a combination of spatial and temporal filtering.

3.4.1. Spatial Filtering

Spatial filtering was applied directly in the spherical harmonic domain to the model parameters $g_{n,k}^m$ and $h_{n,k}^m$ as follows

1. Coefficients with spherical harmonic degree $n \leq 18$ (corresponding to wavelengths longer than 2200 km at Earth's surface) were set to zero.
2. Coefficients with spherical harmonic degree $n \geq 29$ (corresponding to wavelengths shorter than 1,380 km at Earth's surface) were set to zero
3. Coefficients with spherical harmonic order $m \leq 5$ (i.e., near zonal coefficients) were set to zero.
4. Coefficients with spherical harmonic order $m = n$ (i.e., sectoral coefficients) were set to zero.

21699291, 2026, 11, Downloaded from https://agupubs.onlinelibrary.wiley.com/doi/10.1029/2026JC024496 by Christopher Finlay - Danish Technical Knowledge , Wiley Online Library on [12/11/2026]. See the Terms and Conditions (https://onlinelibrary.wiley.com/terms-and-conditions) on Wiley Online Library for rules of use; OA articles are governed by the applicable Creative Commons License

21699291, 2026, 11, Downloaded from https://agupubs.onlinelibrary.wiley.com/doi/10.1029/2026JC024496 by Christopher Finlay - Danish Technical Knowledge , Wiley Online Library on [12/11/2026]. See the Terms and Conditions (https://onlinelibrary.wiley.com/terms-and-conditions) on Wiley Online Library for rules of use; OA articles are governed by the applicable Creative Commons License

The rationale behind these choices was: (a) there was evidence of leakage from imperfectly modeled core signals at low spherical harmonic degrees, as expected based on the spatial spectra of simulated core and oceanic signals (Finlay et al., 2024), (b) the estimated high degree signals ($n > 28$) showed evidence of instability in their power spectra, see Figure 3, and in maps (not shown) (c) unmodelled ionospheric and related induced signals vary with local time so map primarily into the zonal and near zonal coefficients, this was particular evident at auroral and sub-auroral quasi-dipole latitudes, (d) the estimated models possessed noticeable noise in north-south orientated features, which appear most prominently in the sectoral harmonics at low latitudes, likely due either to imperfect magnetospheric or induced field corrections, or instability due to insufficient or missing satellite tracks that were removed in some regions due to the applied quiet-time data selection.

In some cases, in order to aid global visualization and interpretation, when plotting model predictions at Earth surface, masks were applied setting to zero the field outside the tropical region (latitudes above 30°) and over continents, based on height being above sea level on a 1° × 1° topography grid smoothed by a 5° × 5° moving average filter.

3.4.2. Temporal Filtering

In this study the focus of attention is annual variations in the OIMF. This is motivated by the strong annual signal found in simulations of the OIMF (Finlay et al., 2024; Manoj et al., 2006; Stephenson & Bryan, 1992), that is particularly prominent in the Tropical Indian ocean. To isolate the annual variation, which is a broad spectral peak rather than a sharp line as a result of year-to-year variability, we applied temporal filtering designed to retain the signal in a 300–430 days passband.

We first removed the mean value of the time series of each spherical harmonic coefficient (i.e., $g_n^m(t)$ and $h_n^m(t)$), then applied a forward-backward time-domain convolution implementation of a 2nd order Butterworth filter, using the scipy.signal python package's 'filtfilt' function. The combined action of the forward-backward filter is 4th order and it is by construction a zero phase filter. To minimize warm-up transients, initial conditions for the discrete filtering operations were set according to the method of Gustafsson (1996).

4. Results

In this section we report on our OIMF estimates obtained from *Swarm* satellite observations using the method described above, focusing on the band-limited signal associated with annual variations and spherical harmonic degrees 19 to 28. To assess our results we compare to OIMF signals in the same spatio-temporal band from an advanced numerical simulation of the OIMF, described in Section 4.1. In Section 4.2 we report the fit of the derived time-dependent internal field model to the input *Swarm* satellite data and present global spatial spectra for the field model. In Section 4.3 we present an overview of the retrieved signal in the tropical oceans, Sections 4.4–4.7 give detailed comparisons for specific ocean basins.

4.1. Numerical Simulations of OIMF

The simulated OIMF is obtained by solving the electromagnetic induction equation with internal forcing (Finlay et al., 2024; Velímský, 2025),

$$\nabla \times \left(\frac{1}{\sigma} \nabla \times \mathbf{B} \right) + \mu_0 \frac{\partial \mathbf{B}}{\partial t} = \mu_0 \nabla \times (\mathbf{v} \times \mathbf{B}^{\text{core}}), \tag{21}$$

where $\sigma = \sigma(\mathbf{r}; t)$ is the electrical conductivity, $\mathbf{v}(\mathbf{r}; t)$ is the ocean flow velocity, μ_0 is the magnetic permeability, and $\mathbf{B}^{\text{core}}(\mathbf{r}; t)$ is the IGRF13 model of the magnetic field generated by the core (Alken et al., 2021). We take as input ocean flows, temperatures, and salinities from the Copernicus CMEMS mean ocean model (CMEMS, 2024), which is derived from an ensemble of three underlying ocean models. The electrical conductivity of seawater is obtained from CMEMS 4-D climatologies of temperature and salinity, using the thermodynamic equation of seawater (IOC, SCOR and IAPSO, 2010). A compaction and thermal gradient model (Grayver, 2021) describes the conductivity of ocean sediments, while the conductivity of the continental and oceanic lithosphere, underlying mantle, and core follows the 1-D radial profile `MIN_1DM_501`, an ESA *Swarm* Level 2 product obtained by joint inversion of tidal and magnetospheric responses (Grayver et al., 2017). The

21699291, 2026, 11, Downloaded from https://agupubs.onlinelibrary.wiley.com/doi/10.1029/2026JC024496 by Christopher Finlay - Danish Technical Knowledge , Wiley Online Library on [12/11/2026]. See the Terms and Conditions (https://onlinelibrary.wiley.com/terms-and-conditions) on Wiley Online Library for rules of use; OA articles are governed by the applicable Creative Commons License

lateral resolution of the ocean model is reduced to 0.5° × 0.5°, and the spherical harmonic series representing the magnetic field are truncated at degree 240 when solving the induction equation. The radial discretization follows the 75 layers used in the CMEMS model inside the ocean, the total number of layers including the solid Earth reaches 177. The simulated daily OIMF values span the period 2013.0–2023.0, starting from a stationary solution of (21) at 2013.0. A detailed analysis of this numerical simulation, including the sensitivities to input data sets, is beyond the scope of the present study, and will be published elsewhere. Apart from the limits of numerically tractable spatial and temporal resolution, and assuming that only the core field is important for the motional induction, no other physical approximations are used. The solution contains both the poloidal and toroidal modes, consistently treating the galvanic and inductive coupling between the ocean and the underlying solid domains, and realistic bathymetry is implicitly included in the discretization of the conductivity and velocity fields. In the results presented below we apply the same spatio-temporal filtering to the simulation output as that applied to the observation-based field model, and we focus again on the time-interval 2018.5 to 2020.5. Note however that the simulated results should be considered only as a guide to a plausible OIMF and certainly not the true OIMF; due to uncertainties in the underlying ocean-parameters and electrical conductivities of the Earth, there are inherent uncertainties in any simulated OIMF (Irrgang et al., 2016).

A comprehensive representation of the internal forcing in the magnetic induction Equation 21 is the imposed electric current density

$$\mathbf{j}_L = \sigma (\mathbf{v} \times \mathbf{B}^{\text{core}}). \tag{22}$$

To support our later discussion of OIMF observations in the Indian Ocean, we present $\mathbf{j}_L$ in the near-surface layer in the Indian Ocean in Figure 2, after applying the annual bandpass filter in the time domain, but without any spatial domain filtering. The seasonal alternating directions between the Winter and Summer Monsoon Currents, the Somali Current, and the West and East India Coastal Currents (Shankar et al., 2002) are clearly imprinted on all three components of the forcing. Note that $\mathbf{j}_L$ is not restricted by a divergence-free constraint or boundary conditions on the surface, as these apply only to the total electric current density. Indeed, we find the largest annual variations in the simulated radial component along the Somali coast and south of Sri Lanka, which mainly affects the toroidal OIMF component that is not directly observable on or above the ocean surface. However, annual variation of the horizontal imposed currents is also clearly present; these are responsible for the corresponding variations of the OIMF radial component. We note that annual variations of the forcing have a very different spatial structure to the stationary (long-term average) component, which is dominated by the interaction of the Antarctic Circumpolar Current with the radial core field in the southern polar areas, that leads to two prominent patches of opposite signs in the radial component of the OIMF (Manoj et al., 2006; Velímský et al., 2019).

4.2. Fit to Satellite Data and Field Model Spatial Power Spectra

We now turn to results for the field model estimated from the satellite data. Table 2 collects residual statistics for the misfit between the estimated internal field model and the *Swarm* satellite data used to construct it. The Huber-weighted rms misfit to the vector field differences at non-polar latitudes was of order 0.30 nT for the radial and southward components and slightly higher, 0.42 nT, for differences of the east-west component. The amplitude of these misfits reflects the magnitude of unmodelled fields remaining in the corrected data, that cannot be fit by our internal field model and indicate a satisfactory fit to the *Swarm* satellite data.

Spatial (Lowes-Mauersberger) power spectra of the estimated field model, for the unfiltered field and after filtering to retain the annual band (300–430 days) are presented in Figure 3 along with similar spectra for the simulated OIMF truncated at spherical harmonic degree 30, which are shown for reference. The levels of the spectra for the unfiltered and annual-band filtered fields are in approximate agreement between the observation-based field model and the simulated signal; this is by construction and was achieved by adjustment of the hyper-parameters λ_0 and λ_3 respectively, see Sect. 3.3. Some non-oceanic fields are certainly still present in the estimated model, particularly before filtering, in the polar regions and at low spherical harmonic degree. The chosen regularization suppresses the amplitude of these leakage signals, but also damps the estimated OIMF, especially in regions where it is strong.

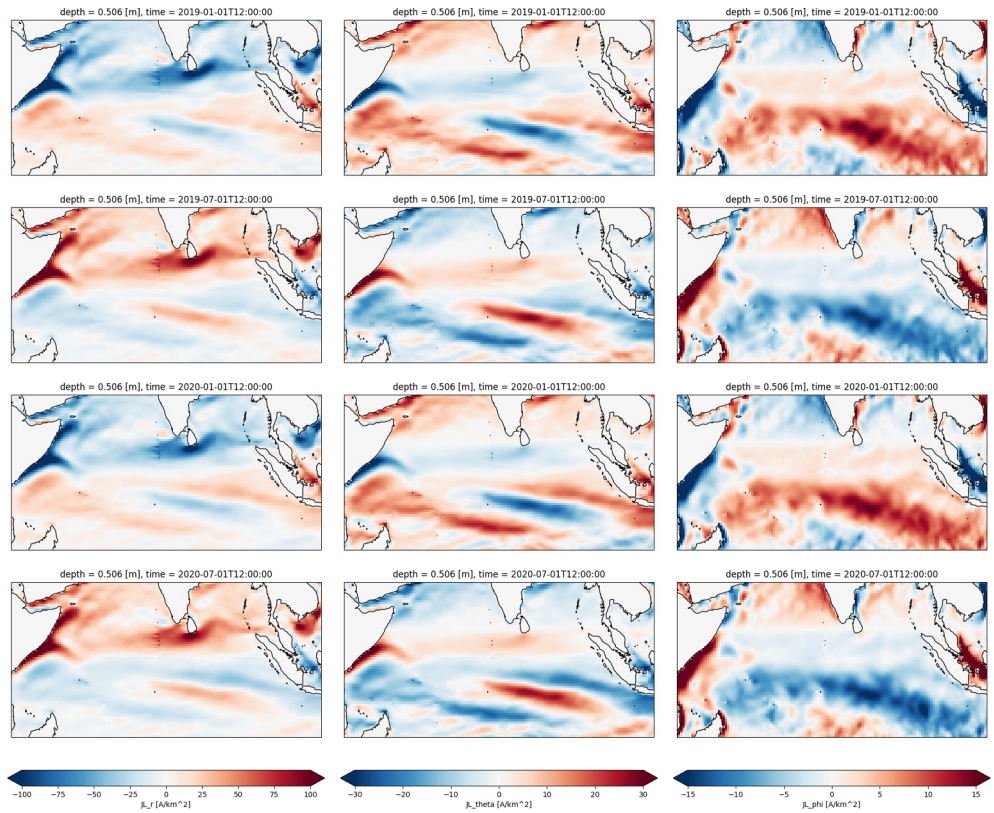


Figure 2. Internal forcing for the simulated ocean-induced magnetic field in the uppermost ocean layer (depth 0.506 m) in the Indian Ocean, due to the imposed electric current density $\mathbf{j}_L$. Radial, meridional, and zonal components are shown respectively in the left, center, and right columns, while the rows correspond to dates 2019-01-01, 2019-07-01, 2020-01-01, and 2020-07-01, respectively top to bottom. Annual filtering in the period band 300–430 days was applied pointwise to individual components.

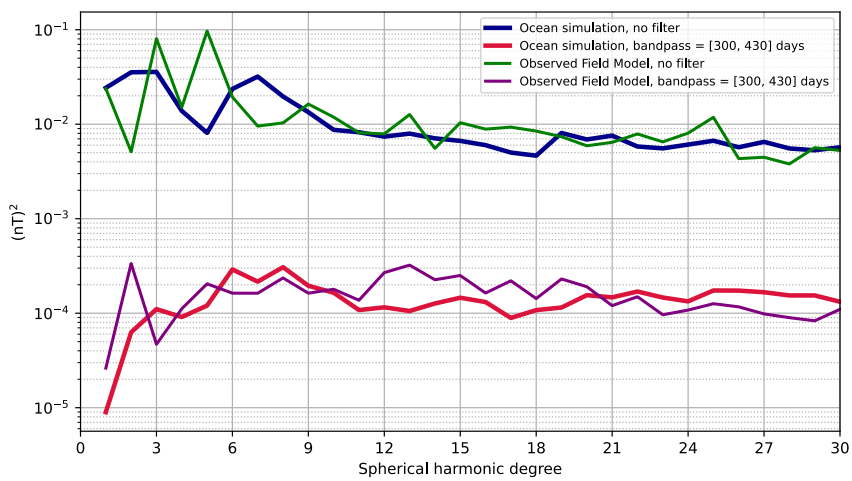


Figure 3. Time-averaged Lowes-Mauersberger spatial power spectra showing the mean squared intensity of the vector magnetic field at Earth's surface as a function of spherical harmonic degree, between degrees 1 and 30. Spectra are presented for the ocean induced magnetic field simulation (thick blue and red lines) and the 'Observed' field model estimated here from the *Swarm* satellite data (green and purple lines), without any temporal filtering applied (upper curves) and band-pass filtered to highlight the annual period band, 300–430 days (lower curves).

21699291, 2026, 11, Downloaded from https://agupubs.onlinelibrary.wiley.com/doi/10.1029/2026JC024496 by Christopher Finlay - Danish Technical Knowledge , Wiley Online Library on [12/11/2026]. See the Terms and Conditions (https://onlinelibrary.wiley.com/terms-and-conditions) on Wiley Online Library for rules of use; OA articles are governed by the applicable Creative Commons License

21699291, 2026, 11, Downloaded from https://agupubs.onlinelibrary.wiley.com/doi/10.1029/2026JC024496 by Christopher Finlay - Danish Technical Knowledge , Wiley Online Library on [12/11/2026]. See the Terms and Conditions (https://onlinelibrary.wiley.com/terms-and-conditions) on Wiley Online Library for rules of use; OA articles are governed by the applicable Creative Commons License

Table 2
Residual Statistics for the Constructed Internal Field Model

Data type	N	$\sigma_{(\delta B_r)}$ [nT]	$\sigma_{(\delta B_\theta)}$ [nT]	$\sigma_{(\delta B_\phi)}$ [nT]	$\sigma_{(\delta F)}$ [nT]
Vector diffs	2,842,922	0.2969	0.3005	0.4227	
Scalar diffs	4,177,461				0.4529

Note. Corrections were applied to the satellite data as described in Section 3.2. N is the number of data of each type (vector or scalar field differences), $\sigma_{(\delta B_r)}$, $\sigma_{(\delta B_\theta)}$ and $\sigma_{(\delta B_\phi)}$ are Huber weighted rms misfits between the model predictions and the radial, southward and eastward components of the *Swarm* satellite vector field, considering both Along-Track and East-West differences (in units nT), $\sigma_{(\delta F)}$ are the Huber-weighted rms misfits between the model predictions and the scalar anomaly field intensity Along-Track and East-West differences (in units nT).

In an effort to minimize the leakage of non-core signals, we hereafter focus on results obtained during the solar minimum time interval of 2018.5–2020.5. The magnetospheric and ionospheric disturbances were in general weaker during this time, and there were more times satisfying our geomagnetic quiet-time selection criteria, resulting in the best opportunity for observing the OIMF.

4.3. Overview of Estimated OIMF in Tropical Oceans and Diagnostics

The estimated internal field model was filtered as described in Sect. 3.4 in order to highlight annual variations at spherical harmonic degree 19 to 28, where the OIMF signal was expected to be accessible. Figure 4 presents two example snapshots, covering all tropical oceans, for 1st July 2019 and 1st April 2020. Snapshots from the same dates from the simulated OIMF are also presented for comparison. The observed signal was here scaled by a factor 2.0 to aid comparison with the simulated signal, and to counteract the loss of amplitude caused by the model regularization.

Strong OIMF signals are found, in both the observed and simulated fields, in the north-western and south-eastern Indian ocean on 1st July 2019. On 1st April 2020, similar OIMF signals are found in the observed and simulated fields in the tropical north-west Atlantic and in the western Pacific. The observed OIMF signal is however in general less well organized, likely due to the leakage of noise in some regions, particularly where the OIMF is weaker. For example, features in the observed OIMF in the eastern Pacific, running west from Mexico are absent from the simulated signal.

The region of most obvious agreement between the observed and simulated signals is the western Indian ocean. Although the signal estimated from the observations is weaker, field structures located east of Somali, in the Arabian Sea, and south of India, share similar spatial structures and time-dependence. These Indian ocean OIMF patterns are discussed in more detail below in Sections 4.4 and 5.

In the tropical Pacific Ocean the simulated OIMF signal, in this spatio-temporal band, appears generally weaker in eastern Pacific and stronger in the western Pacific; this is not obvious in the observed OIMF. The observed OIMF includes noticeable north-south oriented features west of Mexico that are absent in the simulations; we suspect these to be a result of leakage of external field, or associated induced, signals. There are nonetheless hints of agreement in some locations, in the central Pacific around 10 to 15°S in the Samoan Basin and eastwards toward the Marquesas Islands (180°W to 150°W), at low latitudes near Christmas Island (Kiritimati) at 1°N, 157°W, and in the western Pacific close to Vanuatu (around 15°S, 165°E); the agreements in these locations are most easily seen in the time-dependence of the signals. Pacific ocean OIMF patterns are discussed in more detail in Sect. 4.5.

In the Atlantic ocean, the simulated OIMF in the investigated spatio-temporal band is again much weaker than that predicted in the Indian Ocean. Notable features are nevertheless seen in both the observed and simulated OIMF, for example, in the 1st April 2020 snapshot, in the tropical north Atlantic between northern Africa and Florida. Prominent north-south oriented features between Southern Africa and Brazil in the observed OIMF are absent in the simulated OIMF signal. Atlantic ocean OIMF patterns are discussed further in Section 4.6.

The global scaling factor of 2.0 applied to the observed OIMF in this first comparison across all tropical oceans is certainly inadequate. The effect of the regularization is to more strongly suppress the radial field amplitude where it is largest. In the more detailed results presented below for each ocean basin, we estimate and apply a rescaling factor S for each region of the form

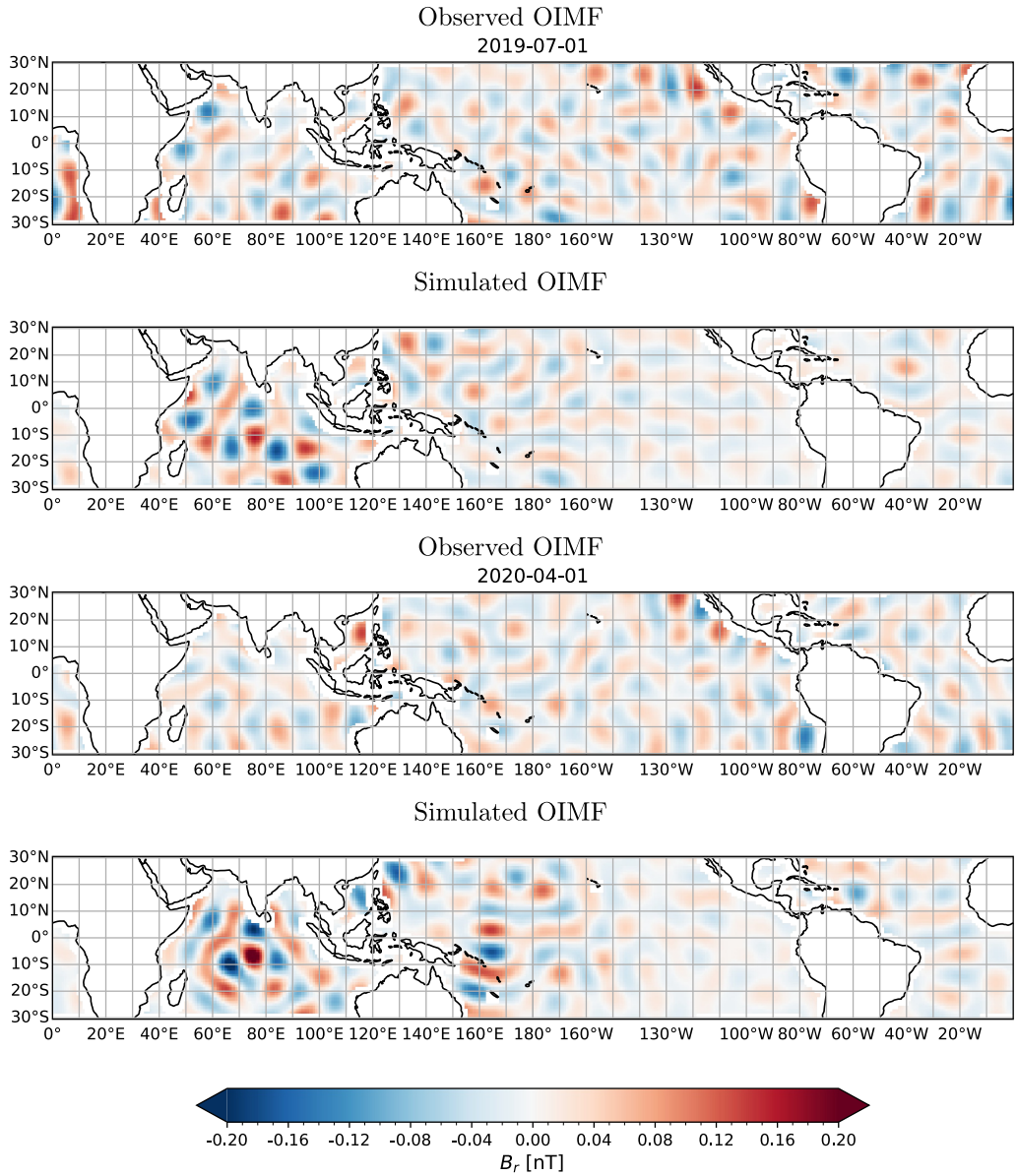


Figure 4. Band-limited ocean induced magnetic field (OIMF) in the tropical oceans estimated from *Swarm* observations (top and third rows for 1st July 2019 and 1st April 2020 respectively) and for the simulated OIMF (second and bottom rows for 1st July 2019 and 1st April 2020 respectively). Presented is the radial field component at Earth's mean surface radius, bandpass filtered to retain the annual period band covering 300–430 days, for spherical harmonic degrees 19 to 28, orders $m = 6$ and above but with the $m = n$ sectoral harmonics excluded. The amplitude of the observed field has been scaled by a factor 2 to aid comparison with the simulated field. The field over the continents have been masked.

$$\widehat{B}^{sc}_{oi,r} = S \cdot \widehat{B}_{oi,r} \tag{23}$$

such that the rms of $\widehat{B}^{sc}_{oi,r}$ in the region considered is the same as that found in the simulation. We report values for S for each region below.

For each considered spatial region or space-time section we also compute correlation coefficients between the filtered simulations and the OIMF estimated from the observations. These are computed as

21699291, 2026, 11, Downloaded from https://agupubs.onlinelibrary.wiley.com/doi/10.1029/2026JC024496 by Christopher Finlay - Danish Technical Knowledge , Wiley Online Library on [12/11/2026]. See the Terms and Conditions (https://onlinelibrary.wiley.com/terms-and-conditions) on Wiley Online Library for rules of use; OA articles are governed by the applicable Creative Commons License

$$C = \frac{\sum_{i=1}^{N_p}\left(\widehat{B}_{oi,r}^{sc} - \bar{B}_{oi,r}^{sc}\right)\left(B_{oi,r}^{sim} - \bar{B}_{oi,r}^{sim}\right)}{\sqrt{\sum_{i=1}^{N_p}\left(\widehat{B}_{oi,r}^{sc} - \bar{B}_{oi,r}^{sc}\right)^2 \sum_{i=1}^{N_p}\left(B_{oi,r}^{sim} - \bar{B}_{oi,r}^{sim}\right)^2}} \tag{24}$$

where $\bar{B}_{oi,r}$ is the mean value of $\widehat{B}_{oi,r}$ in the region considered, $B_{oi,r}^{sim}$ is the filtered OIMF from the simulation, $\bar{B}_{oi,r}^{sim}$ its mean value in the region considered and N_p is the number of pixels in each image.

We also report below an estimate of the number of degrees of freedom D_f in each considered region or time-longitude section, including the impact of the applied spatial and temporal filtering. For a geographical region of area A_{reg}, compared to the area of the full sphere $4\pi r_e^2$, the number of degrees of freedom in the region may be computed as

$$D_f^{\text{reg}} = \frac{A_{\text{reg}}}{4\pi r_e^2} \cdot \left[N_{\max}(N_{\max}+2) - (N_{\min}-1)(N_{\min}+1) - M_{\text{out}}\right] \tag{25}$$

where $N_{\max}$ is the maximum spherical harmonic degree considered, $N_{\min}$ the minimum spherical harmonic degree considered and $M_{\text{out}} = (N_{\max} - N_{\min} + 1)\cdot(2(M_{\min} - 1) + 1)$ where $M_{\min}$ is the minimum considered spherical harmonic order. For example, with $N_{\max} = 28$, $N_{\min} = 19$, $M_{\min} = 6$ we have $M_{\text{out}} = 100$ and $D_f = 370$ for the full sphere.

For a time-longitude section we estimate the number of degrees of freedom as

$$D_f^{TL} = (M_{\max} - M_{\min} + 1) \cdot \frac{\Delta\phi}{360} \cdot 2BT \tag{26}$$

where $M_{\max}$ and $M_{\min}$ are the maximum and minimum considered spherical harmonic orders, $\Delta\phi$ is the range of considered longitudes in degrees, T is the considered timespan in days and B is the temporal bandwidth in units 1/days.

To obtain confidence intervals and p-values for the Correlation Coefficients we computed Correlation Coefficients for 5,000 prior and posterior realizations of our field models. The posterior realizations were obtained from the mean estimated model defined in (20) and its associated model covariance matrix $\underline{\underline{\mathbf{C}}}_{\mathbf{m}} = \left[\underline{\underline{\mathbf{G}}}^{\mathrm{T}}\underline{\underline{\mathbf{W}}}\,\underline{\underline{\mathbf{G}}} + \underline{\underline{\Lambda}}\right]^{-1}$ where $\underline{\underline{\Lambda}} = \left(\lambda_0\underline{\underline{\Lambda}}_0 + \lambda_2\underline{\underline{\Lambda}}_2 + \lambda_3\underline{\underline{\Lambda}}_3\right)$. The prior realizations were obtained using a mean prior model of zero and the prior covariance matrix $\underline{\underline{\mathbf{C}}}_{\mathbf{m_0}} = \underline{\underline{\Lambda}}^{-1}$. Examples of the resulting prior and posterior distributions, for the Correlation Coefficient to the simulated OIMF, are shown in Figure 12. From these distributions we computed 75% posterior confidence intervals and a "p-value," defined here as

$$p\text{–value} \equiv p\left(C_{\text{prior}} \geq \tilde{C}_{\text{post}}\right) \tag{27}$$

which is the probability that a prior model realization has correlation coefficient C_{prior} as large or larger than $\tilde{C}_{\text{post}}$, the median posterior correlation coefficient.

Table 3 collects the scale factors, correlation coefficients for the estimated (posterior mean) model, the number of degrees of freedom (after filtering), 75% confidence intervals for the correlation coefficients derived from posterior model realizations and p-values as defined above, for various regions and time-longitude sections.

4.4. Tropical Indian Ocean

Figure 5 presents three snapshots of the observed and simulated OIMF zoomed into the tropical Indian ocean region in 2019.0, 2019.5 and 2020.0. The observed field in these plots has been scaled by a factor 4.33, consistent with this being a region of high amplitude OIMF annual variations, which have been especially strongly suppressed by the global regularization of B_r^2. The correlation coefficient over the entire region shown in Figure 5 is a

21699291, 2026, 11, Downloaded from https://agupubs.onlinelibrary.wiley.com/doi/10.1029/2026JC024496 by Christopher Finlay - Danish Technical Knowledge , Wiley Online Library on [12/11/2026]. See the Terms and Conditions (https://onlinelibrary.wiley.com/terms-and-conditions) on Wiley Online Library for rules of use; OA articles are governed by the applicable Creative Commons License

Table 3
Correlation Coefficients, Statistics of Significance, and Scale Factors Between Observed and Simulated OIMF

Region	Latitudes (deg)	Longitudes (deg)	Times	Correl Coeff C	Confid int for C (75%)	Degrees of freed. D_f	p-value $p(C_{\text{prior}} \geq \tilde{C}_{\text{post}})$	Scale Fact. S	Fig
Indian Ocean	(−15, 15)	(40, 110)	2019.0 2019.5 2020.0	0.30	(0.01, 0.37)	18.62	0.17	4.33	4
Western Indian Ocean	(−10, 10)	(50, 75)	2019.0 2019.5 2020.0	0.42	(−0.04, 0.52)	4.46	0.22	6.53	4
TL Western Indian Ocean	−5	(45, 70)	(2018.5, 2020.5)	0.52	(−0.06, 0.60)	3.53	0.20	5.42	5
TL Eastern Indian ocean	−15	(90, 105)	(2018.5, 2020.5)	0.80	(0.39, 0.79)	2.11	0.05	2.64	6
Pacific Ocean	(−15, 15)	(120, 250)	2019.25 2019.75 2020.25	0.15	(−0.04, 0.22)	34.58	0.27	1.53	7
TL Central Pacific ocean	5	(180, 230)	(2018.5, 2020.5)	0.61	(0.09, 0.57)	7.06	0.10	1.42	8
Atlantic Ocean	(−5, 30)	(280, 360)	2019.25 2019.75 2020.25	0.34	(0.05, 0.36)	24.13	0.11	1.11	9
TL Western Atlantic ocean	30	(285, 320)	(2018.5, 2020.5)	0.53	(0.11, 0.58)	4.94	0.11	1.08	10
Control Reg: Eurasia	(40, 70)	(55, 105)	2019.0 2019.5 2020.0	0.03	(−0.17, 0.31)	7.63	0.46	0.46	–
Control TL: Eurasia	40	(60, 100)	(2018.5, 2020.5)	−0.01	(−0.24, 0.21)	5.64	0.51	0.43	–

modest 0.30, although this increases to 0.42 in the western Indian ocean region (longitudes 50°E to 75°E, latitudes ±10°, centered on the equator). Close examination of the observed and simulated signals (see also Figure 13 which shows annotated features at one epoch) shows that many similar features can be identified in these snapshots, though there are noticeable phase shifts in the positions between the observed and simulated signals which lowers the correlation coefficient.

In both the simulated and observed Indian Ocean snapshots there are coherent south-west to north-east trending features running approximately parallel to the coast east of Somalia up toward the Arabian sea. For example, on 1st July 2019, see the positive feature running from 55°E at 10°S to 68°E at 10°N in both the observed and simulated signals, but shifted slightly to the west in the observed signal. To the north-west is a similar feature with a negative sign. There is a noticeable difference between the observed and simulated signals near the Gulf of Aden where suspiciously strong features are seen in the observed signal. This ringing-type feature is likely an artifact related to the sharp filtering applied in the spherical harmonic domain and perhaps some leakage of non-OIMF Earth-induced signals. A notable east-west oriented positive-negative anomaly pair is seen at 12°S, at 85°E to 100°E in both the observed and simulated OIMF signals at all three considered epochs. This is stronger compared with other nearby features in the observed signal. At 10°S, 65°E to 70°E the observed signal is always noticeably weaker than the simulated signal.

21699291, 2026, 11, Downloaded from https://agupubs.onlinelibrary.wiley.com/doi/10.1029/2026JC024496 by Christopher Finlay - Danish Technical Knowledge , Wiley Online Library on [12/11/2026]. See the Terms and Conditions (https://onlinelibrary.wiley.com/terms-and-conditions) on Wiley Online Library for rules of use; OA articles are governed by the applicable Creative Commons License

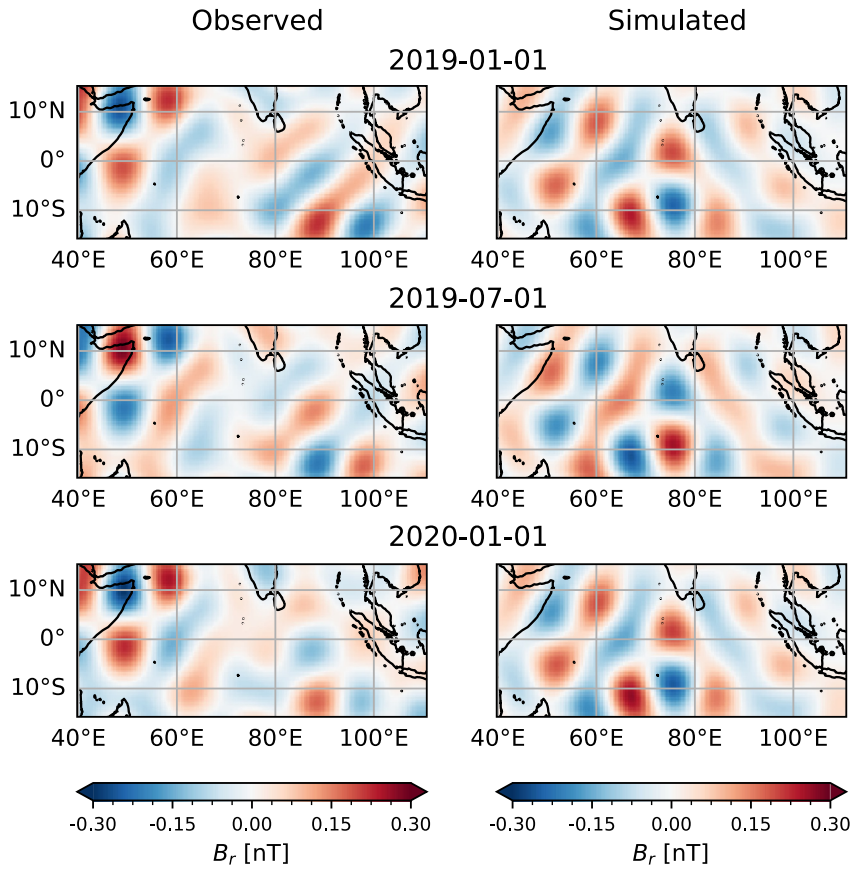


Figure 5. Snapshots of the radial component of the ocean induced magnetic field (OIMF) from the tropical Indian ocean at Earth's surface, left column from the observed signal estimated from *Swarm* data and right column from the OIMF forward simulation. Top row from 1st January 2019, middle row from 1st July 2019 and bottom row from 1st January 2020. Both the observed and simulated signals have been bandpass filtered in time to retain the annual period band covering 300–430 days, and in space to retain spherical harmonic degrees 19 to 28 and orders $m = 6$ and above, but excluding the $m = n$ sectoral harmonics. The observed signal has been scaled by a factor 4.33 to match the rms amplitude of the simulated signal. Correlation coefficient between observed and simulated OIMF averaged over the three epochs is overall 0.30, but increases to 0.42 in the western region (latitudes ±10°N, longitudes 50°E to 75°E). No masking of the signal of the continents has been applied.

Further insight into the similarities between the observed and simulated signals is given by examining their space-time dependence. We do this in Figure 6 and Figure 7 by considering time versus longitude plots of the observed and simulated radial OIMF at two locations where there is obvious east-west dynamics seen in the simulated OIMF signal. Figure 6 focuses on the Western Indian Ocean at 5°S and considers longitudes 45°E to 70°E, running east from Mombasa past the Seychelles to the Mid-Indian Ridge. The simulated OIMF signal in this spatio-temporal band moves consistently eastward in this region throughout the considered interval from 2018.5 to 2020.5. In addition, it shows an intensification near 52°E. The observed OIMF signal in this region also shows clear evidence for eastward propagation with intensifications near 50°E and 57°E. The correlation coefficient between these time-longitude plots is 0.52.

A second comparison of time-longitude plots, this time from the Eastern Indian Ocean at 15°S, running from the Ninety East Ridge that lies east of the Mid-Indian Basin, south of the Cocos Islands over to the West Australian Basin south of the Java trench, is presented in Figure 7. In this region the simulated OIMF signal moves consistently westwards over the studied time interval showing a slight intensification near longitude 94°E. The observed OIMF signal similarly shows clear westward propagation in this region. The spatio-temporal correlation coefficient in this region of persistent westward signal propagation is 0.80.

21699291, 2026, 11, Downloaded from https://agupubs.onlinelibrary.wiley.com/doi/10.1029/2026JC024496 by Christopher Finlay - Danish Technical Knowledge , Wiley Online Library on [12/11/2026]. See the Terms and Conditions (https://onlinelibrary.wiley.com/terms-and-conditions) on Wiley Online Library for rules of use; OA articles are governed by the applicable Creative Commons License

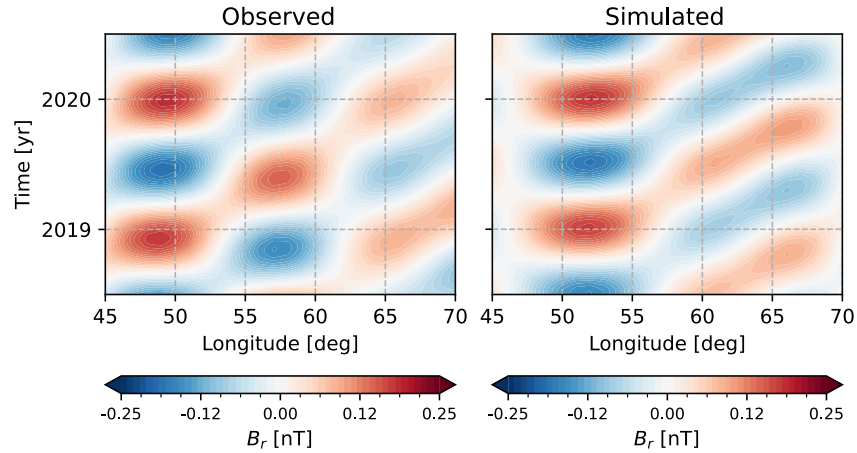


Figure 6. Time-longitude plots of the radial component of the Ocean Induced Magnetic Field (OIMF) from the tropical Indian ocean, at 5°S, and E to 70°E, at Earth's surface, left column for the observed signal estimated from the *Swarm* data and right column from OIMF forward simulation based on the CMEMS mean ocean model. Spatial and temporal filtering is the same as described in Figure 5. The observed signal has been scaled by a factor 5.4 to match the rms amplitude of the simulated signal. The correlation coefficient between observed and simulated OIMF in these time-longitude plots is 0.52.

4.5. Tropical Pacific Ocean

Figure 8 presents three snapshots of the observed and simulated OIMF zoomed into the Pacific ocean region in 2019.25, 2019.75 and 2020.25. The observed field in these plots has been scaled by a factor 1.42, significantly lower than the scaling applied in the Indian ocean, this is consistent with the lower field amplitudes expected in the Pacific and the related weaker impact of the regularization on the amplitudes in this region. The correlation coefficient for the entire tropical Pacific region is a disappointing 0.15, so there is essentially no consistent agreement found between the simulated and observed OIMF. We believe this is a consequence of the overall weaker OIMF signals in this region for the considered spatio-temporal band (the scales in Figure 8 and are a factor 2 smaller than those in Figure 5) so that unmodelled signals and noise dominate the OIMF. There are nevertheless indications of agreement in some specific locations, for example, in the central Pacific around 10 to 15°S in the Samoan Basin and eastwards toward the Marquesas islands (180°W to 150°W), at low latitudes near Christmas Island (Kiritimati) at 1°N, 157°W, and in the western Pacific close to Vanuatu (around 15°S, 165°E). The

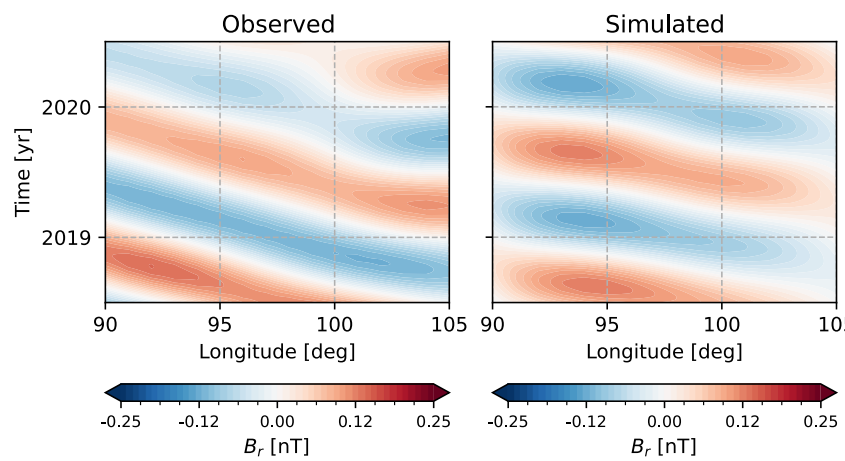


Figure 7. Time-longitude plots of the radial component of the ocean induced magnetic field (OIMF) from the tropical Indian ocean, at 15°S and 90°E to 105°E, at Earth's surface, left column for the observed signal estimated from the *Swarm* data and right column from OIMF forward simulation. Spatial and temporal filtering is the same as described in Figure 5. The observed signal has been scaled by a factor 2.6 to match the rms amplitude of the simulated signal. The correlation coefficient between observed and simulated OIMF in these time-longitude plots is 0.80.

21699291, 2026, 11, Downloaded from https://agupubs.onlinelibrary.wiley.com/doi/10.1029/2026JC024496 by Christopher Finlay - Danish Technical Knowledge , Wiley Online Library on [12/11/2026]. See the Terms and Conditions (https://onlinelibrary.wiley.com/terms-and-conditions) on Wiley Online Library for rules of use; OA articles are governed by the applicable Creative Commons License

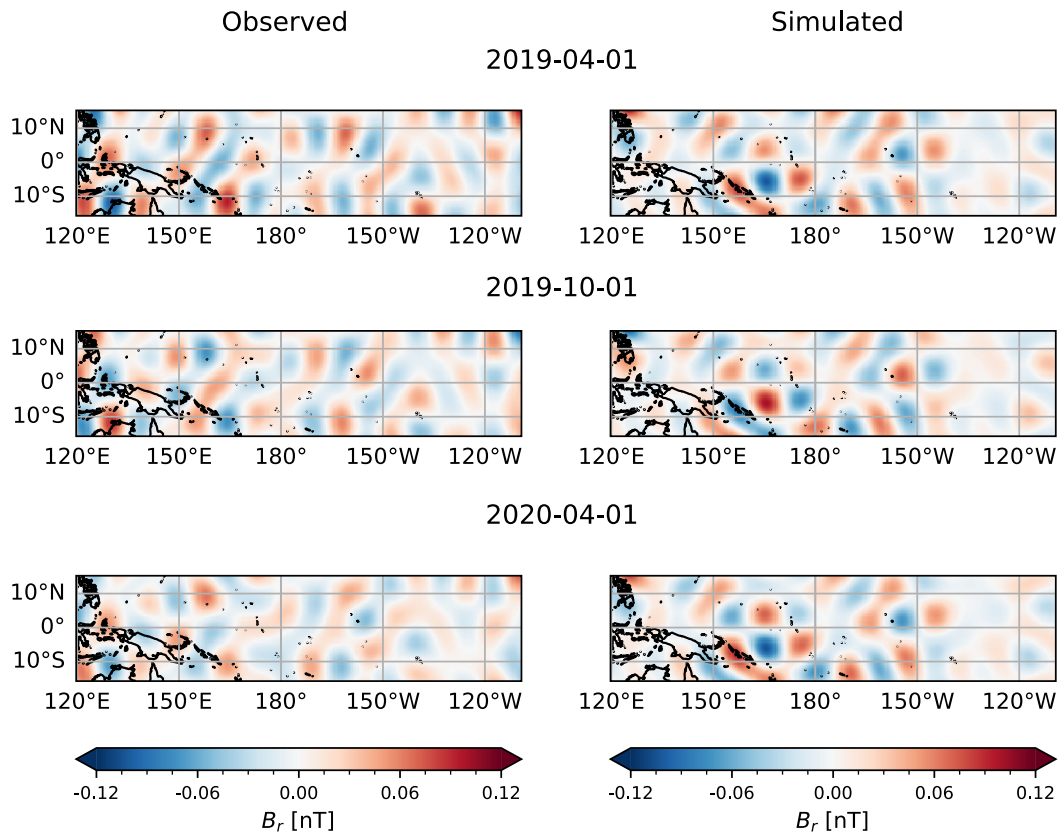


Figure 8. Snapshots of the radial component of the ocean induced magnetic field (OIMF) from the tropical Pacific ocean at Earth's surface, left column for the observed signal estimated from the *Swarm* data and right column from OIMF forward simulation. Top row from 1st April 2019, middle row from 1st October 2019 and bottom row from 1st April 2020. Spatial and temporal filtering is the same as described in Figure 5. The observed signal has been scaled by a factor 1.5 to match the rms amplitude of the simulated signal. No masking of the signal over the continents has been applied. The average correlation coefficient in this region is a disappointing 0.15.

observed signals in the north-eastern tropical Pacific are absent in the simulation and observed signals in the western Pacific have no obvious correspondence with the simulated OIMF.

Figure 9 presents an example time-longitude plot in one of the regions of better agreement, at 5°N and 180°E to 230°E (i.e., 180°W to 150°W). The annual variations between 195°E and 210°E are in good agreement. There are indications of east propagation in the observed OIMF between 180°E and 195°E that are less obvious in the simulated signal, mainly due to a minimum of energy around 185°E. The very simple patterns of variability found in this location (checkerboard-type pattern) indicate that the applied spatio-temporal filtering may be too restrictive here. Further work is needed to study the OIMF in this region over a broader band of spatial wavelengths and periods.

4.6. Tropical Atlantic Ocean

Figure 10 presents three snapshots of the observed and simulated OIMF in the tropical Atlantic ocean region, in 2019.25, 2019.75 and 2020.25. Best agreement between the observed and simulated OIMF signals are found in the region 10°N to 20°N, 70°W to 45°W running from the Caribbean Sea, eastward past the Windward Islands toward the mid-Ocean ridge. There is also good agreement close to 30°N from 75°W to 40°W toward the top left edge of the region shown in these snapshots. The observed signals at 10°N and 30°N at longitudes 75°W to 40°W, seem to be smeared together into diagonal features trending south-west to north-east, while in the simulations they are separated by a node (zero) of the OIMF amplitude near 20°N. Such smearing is likely a result of the regularization applied during the field modeling. In this case the observed signal at all snapshots was scaled by a factor

21699291, 2026, 11, Downloaded from https://agupubs.onlinelibrary.wiley.com/doi/10.1029/2026JC024496 by Christopher Finlay - Danish Technical Knowledge , Wiley Online Library on [12/11/2026]. See the Terms and Conditions (https://onlinelibrary.wiley.com/terms-and-conditions) on Wiley Online Library for rules of use; OA articles are governed by the applicable Creative Commons License

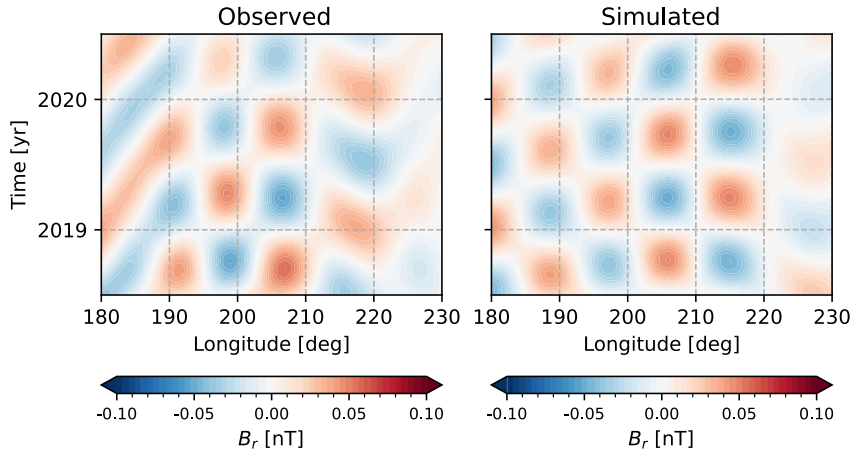


Figure 9. Time-longitude plots of the radial component of the Ocean Induced Magnetic Field (OIMF) from the tropical Pacific ocean, at 5°N and 180°E to 230°E (180°W–130°W), at Earth's surface, left column for the observed signal estimated from the *Swarm* data and right column from the OIMF forward simulation. Spatial and temporal filtering is the same as described in Figure 5. The observed signal has been scaled by a factor 1.4 to match the rms amplitude of the simulated signal, the correlation coefficient for this time-longitude plot is 0.61.

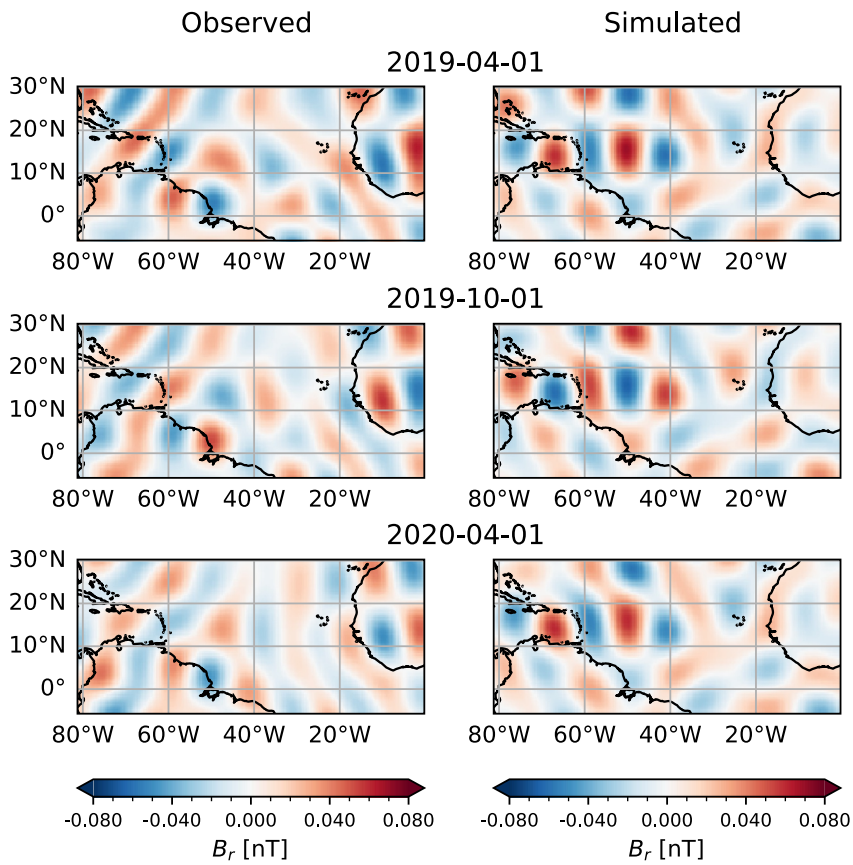


Figure 10. Snapshots of the radial component of the ocean induced magnetic field (OIMF) from the tropical Atlantic ocean at Earth's surface, left column for the observed signal estimated from the *Swarm* data and right column from OIMF forward simulation. Top row from 1st April 2019, middle row from 1st October 2019 and bottom row from 1st April 2020. Spatial and temporal filtering is the same as described in Figure 5. The observed signal has been scaled by a factor 1.1 to match the rms amplitude of the simulated signal. The average correlation coefficient in this region is 0.34. No masking of the signal of the continents has been applied.

21699291, 2026, 11, Downloaded from https://agupubs.onlinelibrary.wiley.com/doi/10.1029/2026JC024496 by Christopher Finlay - Danish Technical Knowledge , Wiley Online Library on [12/11/2026]. See the Terms and Conditions (https://onlinelibrary.wiley.com/terms-and-conditions) on Wiley Online Library for rules of use; OA articles are governed by the applicable Creative Commons License

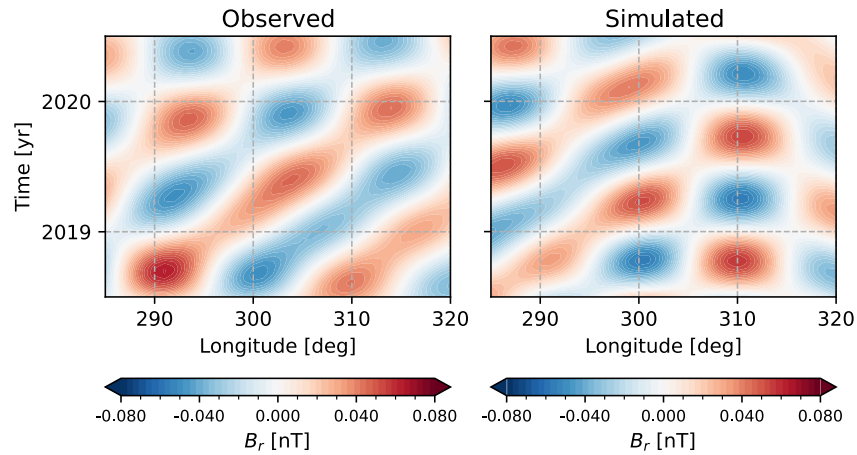


Figure 11. Time-longitude plots of the radial component of the ocean induced magnetic field (OIMF) from the tropical Atlantic ocean, at 30°N and 285°E to 320°E, at Earth's surface, left column for the observed signal estimated from the *Swarm* data and right column from OIMF forward simulation. Spatial and temporal filtering is the same as described in Figure 5. The observed signal has been scaled by a factor 1.08 to match the rms amplitude of the simulated signal. The correlation coefficient between these the observed and simulated space-time signals is 0.53.

of only 1.1, and the correlation coefficient for the whole region was 0.34, so better than in the Pacific, but worse than for the western tropical Indian ocean.

Figure 11 shows an example time-longitude plot from a region where the observed and simulated OIMF signals show evidence of agreement, at latitude 30°N and longitudes 285°E to 320°E (75°W–40°W) running from Florida eastwards to the Mid-Ocean Ridge. In this region the OIMF signals in the studied spatio-temporal band seem to propagate eastwards, in both the observed and simulated cases, moving at a speed of order 15°/yr (approx. 850 km/yr at this latitude). The simulated signal shows patterns more like standing oscillations at longitudes 300°E and 310°E with opposite signs, and with consistently weaker signals at 305°E. In the observed signal, the maxima at 300°E and 310°E appear to be a part of the eastward propagating signal.

4.7. A Negative-Control Region: Eurasia

As an additional test we also computed the observed OIMF signals over a region where no ocean-related signal is expected (i.e., a negative control region), Eurasia. We considered an inland region from latitude 40°N to 70°N and longitude 55°E to 105°E as well as a time-longitude section at latitude 40°N, longitudes 60°E to 100°E and carried out similar comparisons to the simulated OIMF signal. As documented in Table 3 we find very small correlation coefficients in this negative-control region (below 0.05 for both the geographical region and time-longitude plot). The amplitudes of the simulated signal are very small here, less than 0.03 nT; those of the observed field are slightly larger but still very small, less than 0.05 nT.

A more detailed comparison between the correlation coefficients found in the Indian ocean region and the Eurasian negative-control region is presented in Figure 12 This shows probability distributions for the correlation Coefficients between the simulated OIMF and 5,000 prior (orange) and respectively posterior (blue) realizations computed as described in Section 4.3. There are clear differences between the prior and posterior distributions in the Indian Ocean region (left column), with the posterior distribution shifted toward positive correlations to the OIMF simulations. In contrast in the Eurasian negative-control region (right column) there is only a minor difference between the prior and posterior distributions. The top row shows results for geographic regions, the bottom row for time-longitude plots.

The prior realizations here involve random realizations of field models with identical parameterization, the same applied regularization (i.e., a-priori covariances) as used in the field model estimation, and the same filtering applied. By construction these prior realizations are centered on zero correlation and represent realizations of the null hypothesis. The posterior realizations also involve the impact of the satellite observations. The difference between the prior and posterior distributions shows the information gained from the observations regarding the correlation to the OIMF simulations.

21699291, 2026, 11, Downloaded from https://agupubs.onlinelibrary.wiley.com/doi/10.1029/2026JC024496 by Christopher Finlay - Danish Technical Knowledge , Wiley Online Library on [12/11/2026]. See the Terms and Conditions (https://onlinelibrary.wiley.com/terms-and-conditions) on Wiley Online Library for rules of use; OA articles are governed by the applicable Creative Commons License

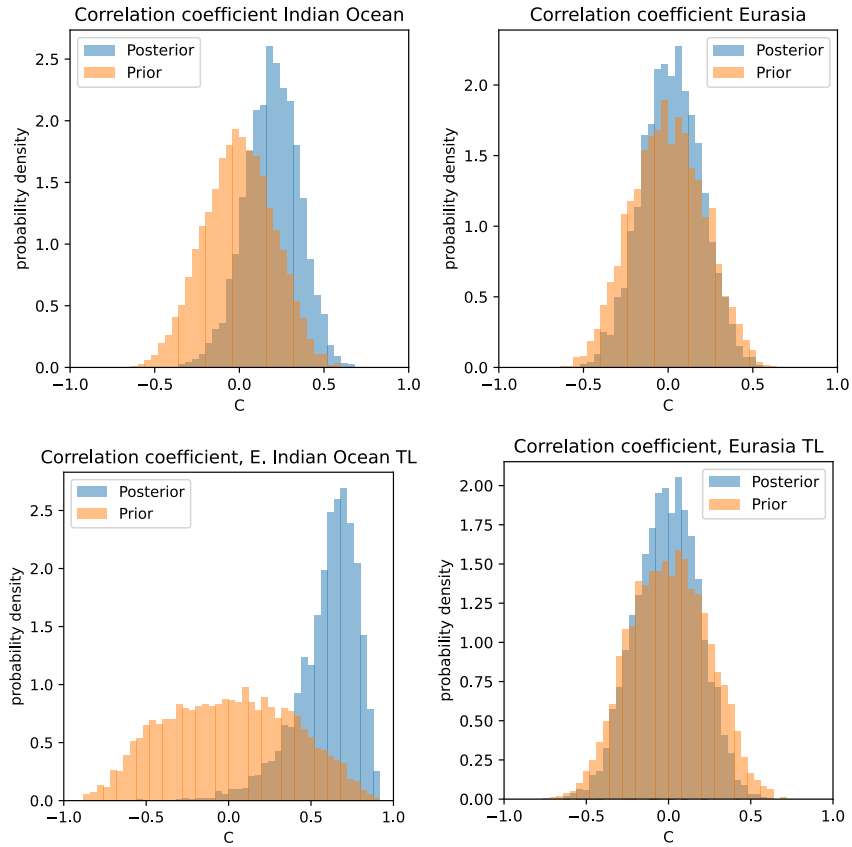


Figure 12. Probability density histograms for correlation coefficients between the simulated ocean induced magnetic field and prior (orange) and respectively posterior (blue) field model realizations. Left column shows result from the Indian ocean region and right column from the Eurasian negative control region. In each case 5,000 model realizations with identical parameterizations were drawn. The prior, posterior and simulated signals each then bandpass filtered, in time to retain the annual period band covering 300–430 days, and in space to retain spherical harmonic degrees 19 to 28 and orders $m = 6$ and above, but excluding the $m = n$ sectoral harmonics.

5. Discussion

The results presented in the previous section provide evidence of moderate localized agreement, in some specific regions, between the OIMF estimated from *Swarm* satellite observations and that predicted by our numerical simulation of the OIMF. We find best agreement in the tropical Indian Ocean, where the simulated OIMF signal is largest. Figure 13 reiterates our results for the observed and simulated radial OIMF in this region in July 2019, now annotated with letters A to K to aid identification of similar field features. Despite a modest correlation coefficient of 0.30, and differences in the relative amplitudes between features, the signs and ordering of the labeled features are in clear agreement. There are however also obvious differences, for example, from 80 to 100°E where south-east to north-west trending features are seen in the simulated but not the observed signal, for example, the feature between *K* and *E* in the simulated signal is absent in the observed signal. In the western Indian ocean the observed features seem to be shifted in space compared to the simulated signals, for example, features A, B are shifted northwards and westwards in the observed signal compared with the simulated signal. Allowing for a single geographic shift over the entire region does however not improve the correlation coefficient. The case for agreement between the observed and simulated signals is strengthened by considering their time-dependence, in particular the coherent patterns of field evolution shown in the time-longitude plots of Figures 6 and 7, in the western and eastern part of the Indian ocean respectively. In our opinion these results indicate that the OIMF related to ocean dynamics has been successfully retrieved in some parts of the tropical Indian ocean.

In the tropical Atlantic Ocean, where the simulated, band-limited, OIMF signal is a factor of two smaller than in the tropical Indian Ocean, the agreement is in general less obvious, although near latitudes 15°N and 30°N from

21699291, 2026, 11, Downloaded from https://agupubs.onlinelibrary.wiley.com/doi/10.1029/2026JC024496 by Christopher Finlay - Danish Technical Knowledge , Wiley Online Library on [12/11/2026]. See the Terms and Conditions (https://onlinelibrary.wiley.com/terms-and-conditions) on Wiley Online Library for rules of use; OA articles are governed by the applicable Creative Commons License

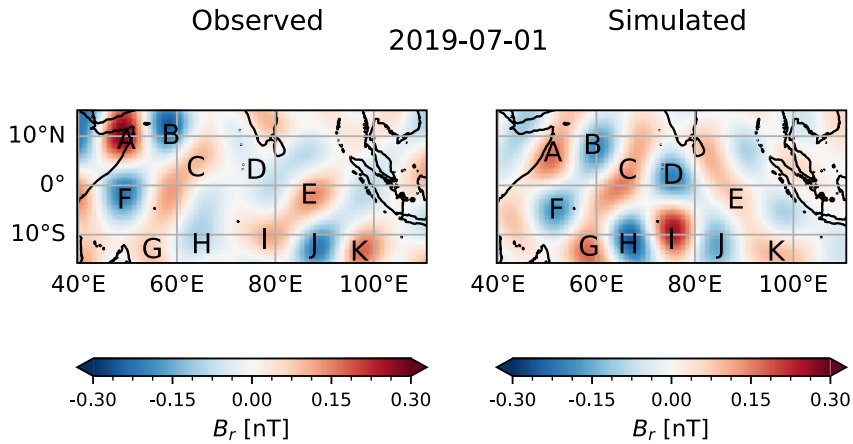


Figure 13. Comparison of observed and simulated ocean induced magnetic field in the Indian ocean region in July 2019, for the period band 300–430 days considering spherical harmonic degrees 19 to 28, orders $m = 6$ and above but excluding the $m = n$ sectoral harmonics. As in Figure 5 but including common features annotated with the letters A to K.

70°W to 40°W (290–320°E), similar features are seen both in snapshots (Figure 10) and in time-longitude plots (Figure 11). The differences between 20°N and 25°N occur where the simulated signal is weaker and the signal estimated from observations seems to have been smeared between the regions of higher field strength. We believe this could be an artifact of the regularization applied during the field modeling. In the Pacific Ocean we find generally poor agreement between the observed and simulated signals (correlation coefficient only 0.15), particularly in the eastern Pacific where the simulated OIMF signal in this spatio-temporal band is weak. There also seems to be more leakage of spurious (non-ocean geomagnetic) signals in this region, perhaps because the magnetospheric field correction model (which is based on ground observatory data) is less reliable, and perhaps because the OIMF signal in this period band has more power at smaller length-scale in this region, making its retrieval more difficult. We did find some localized regions of better agreement, for example, at low latitudes in the central Pacific, although the band-limited OIMF signal in this location was rather monochromatic (dominated by a single wavelength and period, see Figure 9).

When considering the comparisons presented above between the observed and simulated OIMF it is important to remember that the simulated OIMF is not the true OIMF signal. Although based on oceanographic data and using an advanced electromagnetic numerical simulation scheme that includes what are believed to be the relevant physical processes, the simulated OIMF inevitably has some limitations. The ocean flows generating the OIMF are imperfectly known, particularly at depths where the observational sampling is less comprehensive (Irrgang et al., 2016). There is also considerable uncertainty regarding lateral variations in the electrical conductivity at the depths relevant for the 300–430 day periods considered here. It is possible such limitations could contribute to the spatially varying shifts in the OIMF we see between the observed and simulated signals in the Indian Ocean. The OIMF signals discussed here should also be present at ground observatories in ocean regions, for example, on islands. A challenge in this respect is that is not possible to spatially filter the signal from a single ground station and simulations suggest the contribution from small lengthscales to the OIMF measured at Earth's surface can be significant. Nevertheless efforts should be made to see whether specific ground observatories are less influenced by local effects so might be suitable for validation activities.

It is evident that the method employed in this study to estimate the OIMF from satellite data has a number of significant limitations. In an effort to isolate the OIMF signal we applied strong filtering in both space and time. A consequence of this was that both the simulated and observed OIMF were rather monochromatic in some locations. Future studies should strive to extend the considered bandwidth. The spatial filtering was also implemented in a simple way by imposing sharp boundaries in the spherical harmonic domain. Although this is common practise in geomagnetism (e.g. when separating core and lithospheric signals), for the signals considered here, which are not necessarily small outside the chosen bands, it might lead to ringing especially close to sharp ocean-continent boundaries, for example, near to where Somalia meets Gulf of Aden. Use of alternative spatial basis functions that better take account of the geometry of the oceans, and tapering the filters applied in the spherical harmonic domain should help in this regard, once broader bands can be studied. The spatial

21699291, 2026, 11, Downloaded from https://agupubs.onlinelibrary.wiley.com/doi/10.1029/2026JC024496 by Christopher Finlay - Danish Technical Knowledge , Wiley Online Library on [12/11/2026]. See the Terms and Conditions (https://onlinelibrary.wiley.com/terms-and-conditions) on Wiley Online Library for rules of use; OA articles are governed by the applicable Creative Commons License

regularization of B_r^2 imposed during field modeling clearly suppressed high amplitude OIMF features, for example, in the Indian Ocean, while the imposed temporal regularization seems to have caused some over smoothing of signals, especially at higher spherical harmonic degree. More advanced methods of regularization, for example, using prior information on the signal's expected spatio-temporal statistics (see, e.g., Finlay et al., 2025), will be explored in future work.

Where the OIMF signal is small, despite our best efforts, some leakage of unmodelled non-oceanic signals remains. Such leakage is due to limitations in the applied corrections and to signals not included in the corrections. We recommend the external field corrections are also applied to the scalar field anomaly gradients in future studies. Regarding the core field, rapid variations with periods shorter than 2 years are not well modeled by the CHAOS field model and could impact the largest lengthscales and longest timescales of our estimated OIMF, especially in the Pacific region during the period considered here. Regarding the lithospheric field, any time-dependence (real or related to the imperfect spatio-temporal sampling of the satellites) was ignored. Regarding the ionospheric field and associated induced fields, we suspect that the adopted correction models (even after daily rescaling) are not good enough during night-times. Additional restrictions to avoid pre-midnight times where unmodelled F-region currents and plasma bubbles can be present might be beneficial. Regarding the magnetospheric field and related induction in the crust and mantle, improved models of the quiet-time magnetospheric field, for example, with higher time resolution, should lead to improvements, in particular regarding along-track noise. It may also be of interest to attempt to co-estimate a noise model along with the OIMF signal as suggested by Lesur et al. (2013) in the context of crustal field studies.

6. Conclusions

We have presented an algorithm for estimating the general circulation OIMF, by focusing on a limited spatio-temporal bandwidth of 300–430 days and spherical harmonic degrees 19 to 28. We used *Swarm* satellite magnetic field observations, in the form of Along-Track and East-West finite differences, from dark (at mid and low latitudes) and geomagnetic-quiet times, after applying corrections for non-oceanic sources including the core field, crustal field, ionospheric and magnetospheric fields and associated induction in the solid Earth and oceans. A regularized time-dependent field model was fit to the satellite data and the resulting field model spatio-temporally filtered to highlight the band of interest. This observational estimate of the OIMF was compared to a simulated OIMF based on the flows and electrical conductivities from the CMEMS mean ocean model, using realistic couplings to models of the underlying electrically conducting sediments, crust and mantle.

Focusing on the tropics during the solar minimum interval from 2018.5 to 2020.5, we found encouraging agreement between the observed spatio-temporal structures and simulated fields in the Indian ocean, as well as in some parts of the western Atlantic ocean and the central Pacific ocean. Evidence for similar OIMF dynamics, including westward and eastward propagating features, was seen in both the observed and simulated signals in these regions.

Retrieving the inherently small OIMF signal (of order 0.1 nT for the annual variations considered here) nonetheless remains difficult in many regions. We were unable to convincingly retrieve the band-limited OIMF where the simulated OIMF signal was weak, for example, in much of the Pacific Ocean and in the Southern tropical Atlantic Ocean. Best results were restricted to solar minimum conditions when magnetospheric and ionospheric field contributions were weaker and in locations where the OIMF signal in the studied band is largest.

In order to make further progress it is crucial to next extend the spatio-temporal bandwidth of the recovered OIMF. This would enable access to stronger OIMF signals with richer dynamics that can be more easily interpreted in terms of ocean dynamics. For example, extending to higher spherical harmonic degree and shorter periods should allow more details of waves and large-scale eddies to be accessed. Satellite observations from lower altitudes, which are expected from the *Swarm* mission as the lower pair descends, and with faster repeat coverage of geographic locations under geomagnetically quiet and dark conditions, as provided by the low orbital inclination MSS-1 mission (Zhang, 2023) and the upcoming NanoMagSat mission (Hulot et al., 2018), provide an excellent opportunity to make progress here in the next few years. Advances in our knowledge of ionospheric and magnetospheric fields are also expected from the improved local-time coverage provided by MSS-1 and NanoMagSat. This should help mitigate leakage into the estimated OIMF from these sources, and open a path to retrieving the OIMF signal beyond solar minimum conditions and at higher latitudes.

21699291, 2026, 11, Downloaded from https://agupubs.onlinelibrary.wiley.com/doi/10.1029/2026JC024496 by Christopher Finlay - Danish Technical Knowledge , Wiley Online Library on [12/11/2026]. See the Terms and Conditions (https://onlinelibrary.wiley.com/terms-and-conditions) on Wiley Online Library for rules of use; OA articles are governed by the applicable Creative Commons License

21699291, 2026, 11, Downloaded from https://agupubs.onlinelibrary.wiley.com/doi/10.1029/2026JC024496 by Christopher Finlay - Danish Technical Knowledge , Wiley Online Library on [12/11/2026]. See the Terms and Conditions (https://onlinelibrary.wiley.com/terms-and-conditions) on Wiley Online Library for rules of use; OA articles are governed by the applicable Creative Commons License

While efforts to better retrieve the OIMF from satellite observations continue, work in parallel is needed on establishing the benefit such observations can bring, in the form of volume-integrated independent constraints on ocean parameters including velocities, temperatures and salinities. Numerical simulations linking the ocean parameters, such as the ocean conductivity content (conductance) and the depth-integrated conductivity-weighted velocity to OIMF observations, exist (Trossman et al., 2024). The impact on ocean state estimates of assimilating such OIMF observations can be studied by computing adjoint sensitivities, which can then also be used in data assimilation experiments. We have here described annual OIMF signals related to monsoon-driven annual variations in the Indian ocean circulations and in the western north Atlantic related to variations in the Gulf Stream. Further study is needed to determine whether OIMF observations might provide a means of monitoring novel aspects of the related Indian Ocean Dipole or Atlantic Meridional Overturning Circulation systems. Such investigations will require deeper collaborations between geomagnetists and oceanographers.

Appendix A: Tests of Algorithm With Synthetic Satellite Data

This Appendix documents results of an application of our method to synthetic satellite data, where a known ocean signal is input and we test whether the algorithm described in the main text is able to successfully retrieve it.

A1. Synthetic Data

Synthetic satellite data sets were constructed by evaluating known magnetic signals from sources of interest at the times and locations of the *Swarm* satellite data set employed above, using the same dark and quiet-time criteria as described in the main text. We consider two cases. (a) "Ocean-only," where only an OIMF signal was included. This is from the same numerical simulation described above in Section 4.1, with the OIMF signal at satellite altitude computed using interpolated daily spherical harmonics up to degree and order 60. Since this data set is noise-free we allocated very small data errors of 0.001 nT. (b) 'Ocean + noise', in addition to the same OIMF signal used in the previous case, this also includes simulated magnetospheric and ionospheric signals (taken to be 15% of the $\mathbf{B}^{\mathrm{Ext,corr}}$ signal documented in Section 3.2, so effectively imagining this correction to be imperfect). Earth-induced currents are included via the models contributing to $\mathbf{B}^{\mathrm{Ext,corr}}$; at non-polar latitudes these include the impact of lateral variations in the electrical conductivity in a near-surface layer. In addition to these fields driven by external current systems, random isotropic noise of amplitude 0.1 nT was also added. Larger error estimates of 0.2 nT, similar to those used for real data in the main text, were adopted for this more realistic "Ocean + noise" case.

A2. Field Modeling Setup

The time-dependent internal field model fit to both synthetic data sets used an identical parameterization to that described in the main text, with maximum spherical harmonic degree and order 30, sixth order B-splines and 60 days knot spacing. For the noise-free 'ocean-only' model no regularization was applied and estimation was via least-squares without re-weighting. For the 'ocean + noise' data set the same regularization norms (but with $\lambda_0 = 6 \times 10^4 (\mathrm{nT})^{-2}$, $\lambda_2 = 15\left(\mathrm{nT/yr}^2\right)^{-2}$ and $\lambda_3 = 15\left(\mathrm{nT/yr}^3\right)^{-2}$) and iterative (Huber) reweighting was applied in the model estimation as was the case for the real data. The regularization applied here is weaker than that used for the real *Swarm* data, since there is additional (poorly understood) noise/unmodelled signal present in the real data. The regularization parameters were chosen, as for the real data case, by trying to match the level of the OIMF simulation spatial power spectra for both the field and the field in the annual band.

A3. Results

In Figure A1 we present regional maps and in Figure A2 time-longitude plots of the filtered OIMF retrieved from inverting the "Ocean + noise" and "Ocean-only" data sets. Table A1 presents correlation coefficients and scale factors between each and the input OIMF simulation signal. As expected, the input OIMF signal is very well retrieved in the 'Ocean-only' inversion with correlation coefficients higher than 0.94 and scale factors close to 1 in the chosen band of spherical harmonic degrees 19 to 28 and 300–430 days. This demonstrates that our algorithm is able to retrieve the OIMF signal from data collected on the orbits of the *Swarm* satellites, with the dark, quiet time selection criteria applied, from noise-free data.

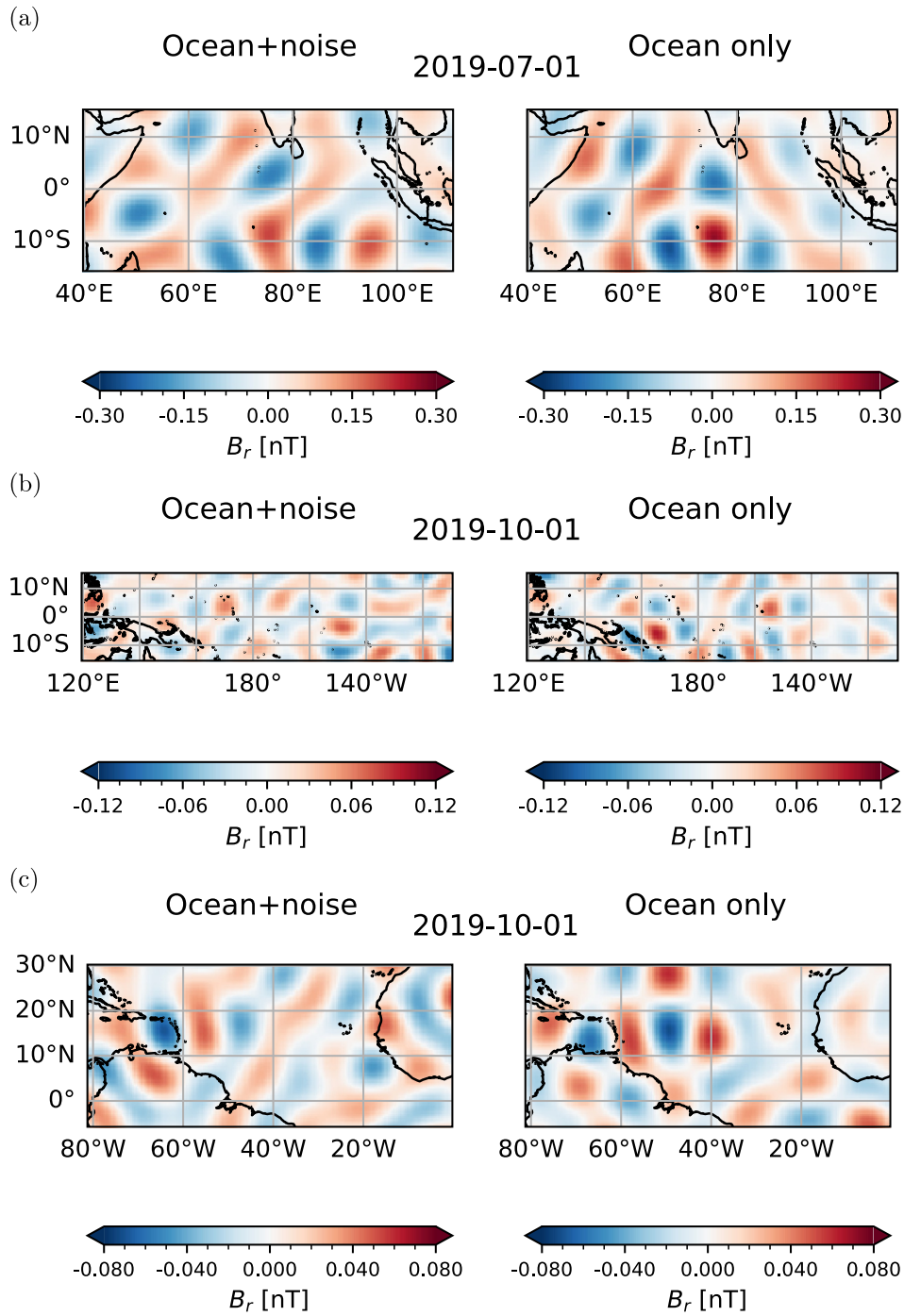


Figure A1. Comparison of regional filtered ocean induced magnetic field from inversion of synthetic satellite data containing only a known ocean signal (right column) and from the same ocean signal plus simulated noise from unmodelled magnetospheric, ionospheric and associated induced fields (left column). (a) For the Tropical Indian Ocean in July 2019, (b) for the Tropical Pacific Ocean in October 2019, (c) for the Tropical Atlantic Ocean in 2019. Spatial and temporal filtering is the same as described in Figure 5. The figures in the left column have been re-scaled by factors 2.13, 1.13 and 0.82 to aid comparisons.

For the model derived from the "Ocean + noise" data set, we find good localized agreement with the input OIMF signal in some regions, for example, in the Indian ocean where correlation coefficients above 0.7 are achieved, although larger scale-factors are needed (as the imposed regularization strongly suppresses the field amplitudes in

21699291, 2026, 11, Downloaded from https://agupubs.onlinelibrary.wiley.com/doi/10.1029/2026JC024496 by Christopher Finlay - Danish Technical Knowledge , Wiley Online Library on [12/11/2026]. See the Terms and Conditions (https://onlinelibrary.wiley.com/terms-and-conditions) on Wiley Online Library for rules of use; OA articles are governed by the applicable Creative Commons License

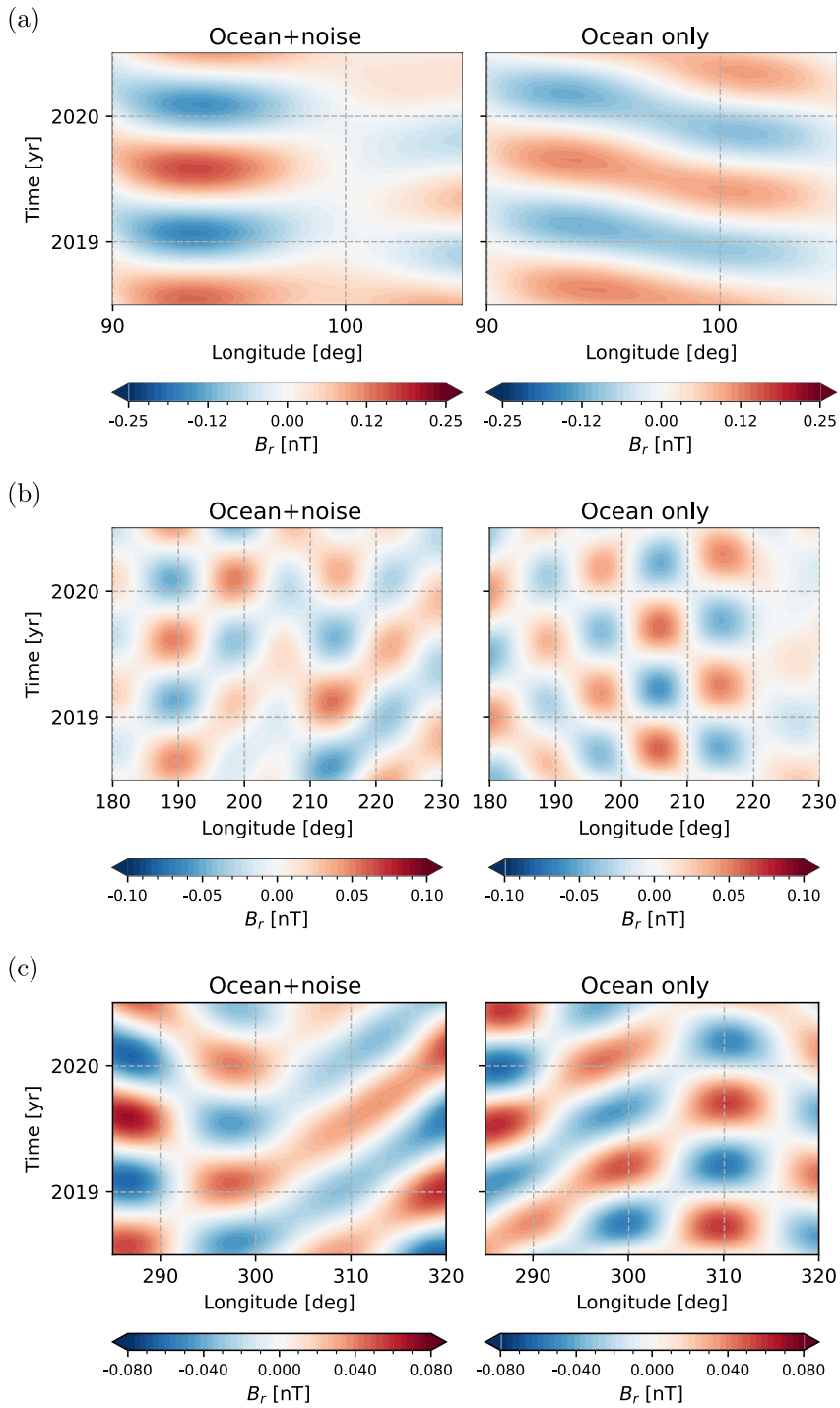


Figure A2. Comparison of time-longitude plots of filtered ocean induced magnetic field from inversion of synthetic satellite data containing only a known ocean signal (right column) and from the same ocean signal plus simulated noise from unmodelled magnetospheric, ionospheric and associated induced fields (left column). Between 2018.5 and 2020.5 (a) for the Tropical Indian Ocean at 15°S, 90°E to 105°E, (b) for the Tropical Pacific Ocean at 5°N, 180°E probably somewhat to 230°E, (c) for the Tropical Atlantic Ocean at 30°N, 285°E to 320°E. Spatial and temporal filtering is the same as described in Figure 5. The figures in the left column have been re-scaled by factors 3.43, 0.76 and 1.34 to aid comparisons.

this region, due to the high amplitudes in the input signal). The retrievals in the Pacific and Atlantic are noticeably worse for the 'Ocean + noise' data set, especially for the regional plots. Clearly the noise has more impact where the OIMF signal is weaker, see for example, the spurious signals seen in the Eastern Pacific where the input OIMF

21699291, 2026, 11, Downloaded from https://agupubs.onlinelibrary.wiley.com/doi/10.1029/2026JC024496 by Christopher Finlay - Danish Technical Knowledge , Wiley Online Library on [12/11/2026]. See the Terms and Conditions (https://onlinelibrary.wiley.com/terms-and-conditions) on Wiley Online Library for rules of use; OA articles are governed by the applicable Creative Commons License

21699291, 2026, 11, Downloaded from https://agupubs.onlinelibrary.wiley.com/doi/10.1029/2026JC024496 by Christopher Finlay - Danish Technical Knowledge , Wiley Online Library on [12/11/2026]. See the Terms and Conditions (https://onlinelibrary.wiley.com/terms-and-conditions) on Wiley Online Library for rules of use; OA articles are governed by the applicable Creative Commons License

Table A1
Correlation Coefficients and Scale Factors Between Inverted "Ocean + noise" and "Ocean Only" Data Sets and Simulated OIMF

Region	Latitudes (deg)	Longitudes (deg)	Times	"Ocean + noise" Correl Coeff C	"Ocean + noise" Scale Fact. S	"Ocean only" Correl Coeff C	"Ocean only" Scale Fact. S
Indian Ocean	(−15, 15)	(40, 110)	2019.0 2019.5 2020.0	0.71	2.07	0.99	0.97
Western Indian Ocean	(−10, 10)	(50, 75)	2019.0 2019.5 2020.0	0.86	2.67	1.00	0.98
TL Western Indian Ocean	−5	(45, 70)	(2018.5, 2020.5)	0.87	2.13	0.99	1.04
TL Eastern Indian Ocean	−15	(90, 105)	(2018.5, 2020.5)	0.81	4.39	0.99	1.02
Pacific Ocean	(−15, 15)	(120, 250)	2019.25 2019.75 2020.25	0.28	1.14	0.98	0.98
TL Central Pacific Ocean	5	(180, 230)	(2018.5, 2020.5)	0.46	0.73	0.97	0.93
Atlantic Ocean	(−5, 30)	(280, 360)	2019.25 2019.75 2020.25	0.12	0.77	0.94	0.94
TL Western Atlantic Ocean	30	(285, 320)	(2018.5, 2020.5)	0.58	1.23	0.97	0.93

signal is weak in the chosen spatio-temporal band. The noise level added in this test is probably somewhat optimistic (note the larger regularization parameters needed to invert the real data), but the results nonetheless give valuable insight into where we may expect to retrieve the OIMF (where its amplitude is large compared with the noise), and where spurious signals from noise might leak and contaminate the estimated OIMF.

Conflict of Interest

The authors declare no conflicts of interest relevant to this study.

Acknowledgments
This work was supported by ESA under the Swarm for Ocean Project, Contract No. 4000143627/24/I-EB, as part of the EO for Society programme. The presented simulations of the ocean-induced magnetic field were supported by the Ministry of Education, Youth and Sports of the Czech Republic through the e-INFRA CZ (ID:90254), project OPEN-30-29. The authors thank Nils Olsen, Alexander Grayver, Lorenzo Trenchi and Roberto Sabia for helpful discussions. Carla Grüne is thanked for providing the function used to order filter the spherical harmonic models. We thank Hongbo Yao and an anonymous reviewer for constructive comments that helped us improve the manuscript.

Availability Statement

The magnetic field models presented above, and the processed magnetic field data sets used to derive these are available from DTU (2025). The OIMF forward simulations are available from CUP (2025). Magnetic field measurements from ESA's *Swarm* satellite trio are available from the European Space Agency (2026). The CMEMS Global Ocean Ensemble Physics Reanalysis, used in the OIMF forward simulations, is available from CMEMS (2024).

References

Alken, P., Thébault, E., Beggan, C. D., Amit, H., Aubert, J., Baerenzung, J., et al. (2021). International geomagnetic reference field: The thirteenth generation. *Earth Planets and Space*, *73*(1), 49. https://doi.org/10.1186/s40623-020-01288-x

CMEMS. (2024). Global ocean ensemble physics reanalysis, E.U. copernicus marine service information (CMEMS), marine data store (MDS). https://doi.org/10.48670/moi-00016

Constable, C. G. (1988). Parameter estimation in non-Gaussian noise. *Geophysical Journal International*, *94*(1), 131–142. https://doi.org/10.1111/j.1365-246X.1988.tb03433.x

CUP. (2025). *Numerical simulations of the ocean circulation induced magnetic field from the Swarm for Ocean Dynamics project, (See run006)*. Charles University. Retrieved from https://owncloud.cesnet.cz/index.php/s/FUlO3PKHzBQpMRN

DTU. (2025). *Magnetic field datasets and field models from the Swarm for Ocean Dynamics project*. (See data files SfOD_OB_XXX and model files SfOD_TDIFM_ XX). Technical University of Denmark. Retrieved from https://www.spacecenter.dk/files/magnetic-models/SfOD/Datasets/

European Space Agency. (2026). Level 1b magnetic field data from the *Swarm* satellite mission. *ESA*. Retrieved from https://swarm-diss.eo.esa.int/(Dataset

Faraday, M. (1832). VI. The Bakerian lecture.-experimental researches in electricity. Second series. *Philosophical Transactions of the Royal Society of London*, *122*, 163–194. https://doi.org/10.1098/rstl.1832.0007

Finlay, C. C., Kloss, C., & Gillet, N. (2025). Core field changes from eleven years of Swarm satellite observations. *Physics of the Earth and Planetary Interiors*, *368*, 107447. https://doi.org/10.1016/j.pepi.2025.107447

Finlay, C. C., Kloss, C., Olsen, N., Hammer, M. D., Tøffner-Clausen, L., Grayver, A., & Kuvshinov, A. (2020). The CHAOS-7 geomagnetic field model and observed changes in the south Atlantic anomaly. *Earth Planets and Space*, *72*(1), 1–31. https://doi.org/10.1186/s40623-020-01252-9

Finlay, C. C., Velímský, J., Kloss, C., & Blangsbøll, R. M. (2024). Satellite monitoring of long period ocean-induced magnetic field variations. *Philosophical Transactions A*, *382*(2286), 20240077. https://doi.org/10.1098/rsta.2024.0077

Friis-Christensen, E., Lühr, H., & Hulot, G. (2006). *Swarm*: A constellation to study the Earth's magnetic field. *Earth Planets and Space*, *58*(4), 351–358. https://doi.org/10.1186/BF03351933

Golubev, Y. (2012). Ocean-generated magnetic field study based on satellite geomagnetic measurements: 2. Signal inference. *Journal of Geophysical Research*, *117*(C9). https://doi.org/10.1029/2012JC007976

Grayver, A. V. (2021). Global 3-D electrical conductivity model of the world ocean and marine sediments. *Geochemistry, Geophysics, Geosystems*, *22*(9), e2021GC009950. https://doi.org/10.1029/2021GC009950

Grayver, A. V., Finlay, C. C., & Olsen, N. (2024). Magnetic signals from Oceanic tides: New satellite observations and applications. *Philosophical Transactions of the Royal Society of London - A*, *382*(2286), 20240078. https://doi.org/10.1098/rsta.2024.0078

Grayver, A. V., Munch, F. D., Kuvshinov, A. V., Khan, A., Sabaka, T. J., & Tøffner-Clausen, L. (2017). Joint inversion of satellite-detected tidal and magnetospheric signals constrains electrical conductivity and water content of the upper mantle and transition zone. *Geophysical Research Letters*, *44*(12), 6074–6081. https://doi.org/10.1002/2017GL073446

Grayver, A. V., & Olsen, N. (2019). The magnetic signatures of the M_2, N_2, and O_1 Oceanic tides observed in Swarm and CHAMP satellite magnetic data. *Geophysical Research Letters*, *46*(8), 4230–4238. https://doi.org/10.1029/2019GL082400

Gustafsson, F. (1996). Determining the initial states in forward-backward filtering. *IEEE Transactions on Signal Processing*, *44*(4), 988–992. https://doi.org/10.1109/78.492552

Hornschild, A., Baerenzung, J., Saynisch-Wagner, J., Irrgang, C., & Thomas, M. (2022). On the detectability of the magnetic fields induced by ocean circulation in geomagnetic satellite observations. *Earth Planets and Space*, *74*(1), 182. https://doi.org/10.1186/s40623-022-01741-z

Huber, P. J. (2004). *Robust statistics*. Wiley.

Hulot, G., Léger, J.-M., Vigneron, P., Jager, T., Bertrand, F., Coïsson, P., et al. (2018). Nanosatellite high-precision magnetic missions enabled by advances in a stand-alone scalar/vector absolute magnetometer. In *Igarss 2018 - 2018 IEEE international geoscience and remote sensing symposium* (pp. 6320–6323).

IOC, SCOR, & IAPSO. (2010). The international thermodynamic equation of seawater - 2010: Calculations and use of thermodynamic properties. *Intergovernmental Oceanographic Commission, Manuals and Guides No. 56, UNESCO (English)*.

Irrgang, C., Saynisch, J., & Thomas, M. (2016). Ensemble simulations of the magnetic field induced by global ocean circulation: Estimating the uncertainty. *Journal of Geophysical Research: Oceans*, *121*(3), 1866–1880. https://doi.org/10.1002/2016JC011633

Irrgang, C., Saynisch-Wagner, J., & Thomas, M. (2018). Depth of origin of ocean-circulation-induced magnetic signals. *Annales Geophysicae*, *36*(1), 167–180. https://doi.org/10.5194/angeo-36-167-2018

Kloss, C., Finlay, C. C., Olsen, N., Tøffner-Clausen, L., Gillet, N., & Grayver, A. (2026). The CHAOS-8 geomagnetic field model. *Earth Planets and Space*, *78*(21), 21. https://doi.org/10.1186/s40623-025-02352-0

Larsen, J. (1968). Electric and magnetic fields induced by deep sea tides. *Geophysical Journal International*, *16*(1), 47–70. https://doi.org/10.1111/j.1365-246X.1968.tb07135.x

Laundal, K. M., Finlay, C. C., Olsen, N., & Reistad, J. P. (2018). Solar wind and seasonal influence on ionospheric currents from Swarm and CHAMP measurements. *Journal of Geophysical Research: Space Physics*, *123*(5), 4402–4429. https://doi.org/10.1029/2018ja025387

Laundal, K. M., & Richmond, A. D. (2017). Magnetic coordinate systems. *Space Science Reviews*, *206*(1–4), 27–59. https://doi.org/10.1007/978-94-024-1225-3_3

Lesur, V., Rother, M., Vervelidou, F., Hamoudi, M., & Thébault, E. (2013). Post-processing scheme for modelling the lithospheric magnetic field. *Solid Earth*, *4*(1), 105–118. https://doi.org/10.5194/se-4-105-2013

Longuet-Higgins, M. (1949). The electrical and magnetic effects of tidal streams. *Geophysical Journal International*, *5*, 285–307. https://doi.org/10.1111/j.1365-246X.1949.tb02945.x

Manoj, C., Kuvshinov, A., Maus, S., & Lühr, H. (2006). Ocean circulation generated magnetic signals. *Earth Planets and Space*, *58*(4), 429–437. https://doi.org/10.1186/bf03351939

Matzka, J., Stolle, C., Yamazaki, Y., Bronkalla, O., & Morschhauser, A. (2021). The geomagnetic Kp index and derived indices of geomagnetic activity. *Space Weather*, *19*(5), e2020SW002641. https://doi.org/10.1029/2020sw002641

Newell, P. T., Sotirelis, T., Liou, K., Meng, C. I., & Rich, F. J. (2007). A nearly universal solar wind-magnetosphere coupling function inferred from 10 magnetospheric state variables. *Journal of Geophysical Research*, *112*(A1). https://doi.org/10.1029/2006JA012015

Olsen, N., & Floberghagen, R. (2018). Exploring geospace from space: The Swarm satellite constellation mission. *Space Research Today*, *203*, 61–71. https://doi.org/10.1016/j.srt.2018.11.017

Olsen, N., Hulot, G., Lesur, V., Finlay, C. C., Beggan, C., Chulliat, A., et al. (2015). The Swarm initial field model for the 2014 geomagnetic field. *Geophysical Research Letters*, *42*(4), 1092–1098. https://doi.org/10.1002/2014GL062659

Olsen, N., Lühr, H., Finlay, C. C., Sabaka, T. J., Michaelis, I., Rauberg, J., & Tøffner-Clausen, L. (2014). The CHAOS-4 geomagnetic field model. *Geophysical Journal International*, *197*(2), 815–827. https://doi.org/10.1093/gji/ggu033

Olsen, N., Ravat, D., Finlay, C. C., & Kother, L. K. (2017). LCS-1: A high-resolution global model of the lithospheric magnetic field derived from CHAMP and Swarm satellite observations. *Geophysical Journal International*, *211*(3), 1461–1477. https://doi.org/10.1093/gji/ggx381

Sabaka, T. J., Olsen, N., Tyler, R. H., & Kuvshinov, A. (2015). CM5, a pre-Swarm comprehensive geomagnetic field model derived from over 12 yr of CHAMP, Ørsted, SAC-C and observatory data. *Geophysical Journal International*, *200*(3), 1596–1626. https://doi.org/10.1093/gji/ggu493

21699291, 2026, 11, Downloaded from https://agupubs.onlinelibrary.wiley.com/doi/10.1029/2026JC024496 by Christopher Finlay - Danish Technical Knowledge , Wiley Online Library on [12/11/2026]. See the Terms and Conditions (https://onlinelibrary.wiley.com/terms-and-conditions) on Wiley Online Library for rules of use; OA articles are governed by the applicable Creative Commons License

Sabaka, T. J., Tøffner-Clausen, L., Olsen, N., & Finlay, C. C. (2018). A comprehensive model of earth's magnetic field determined from 4 years of swarm satellite observations. *Earth Planets and Space*, *70*(1), 1–26. https://doi.org/10.1186/s40623-018-0896-3

Sabaka, T. J., Tøffner-Clausen, L., Olsen, N., & Finlay, C. C. (2020). CM6: A comprehensive geomagnetic field model derived from both CHAMP and Swarm satellite observations. *Earth Planets and Space*, *72*(1), 1–24. https://doi.org/10.1186/s40623-020-01210-5

Sabaka, T. J., Tyler, R. H., & Olsen, N. (2016). Extracting ocean-generated tidal magnetic signals from Swarm data through satellite gradiometry. *Geophysical Research Letters*, *43*(7), 3237–3245. https://doi.org/10.1002/2016GL068180

Šachl, L., Martinec, Z., Velímský, J., Irrgang, C., Petereit, J., Saynisch, J., et al. (2019). Modelling of electromagnetic signatures of global ocean circulation: Physical approximations and numerical issues. *Earth Planets and Space*, *71*(1), 58. https://doi.org/10.1186/s40623-019-1033-7

Sanford, T. B. (1971). Motionally induced electric and magnetic fields in the sea. *Journal of Geophysical Research*, *76*(15), 3476–3492. https://doi.org/10.1029/JC076i015p03476

Saynisch-Wagner, J., Baerenzung, J., Hornschild, A., Irrgang, C., & Thomas, M. (2021). Tide-induced magnetic signals and their errors derived from CHAMP and Swarm satellite magnetometer observations. *Earth Planets and Space*, *73*, 1–11. https://doi.org/10.1186/s40623-021-01557-3

Saynisch-Wagner, J., Baerenzung, J., Hornschild, A., & Thomas, M. (2023). Tidal transports from satellite observations of Earth's magnetic field. *Scientific Reports*, *13*(1), 13302. https://doi.org/10.1038/s41598-023-40448-3

Shankar, D., Vinayachandran, P., & Unnikrishnan, A. (2002). The monsoon currents in the north Indian Ocean. *Progress in Oceanography*, *52*(1), 63–120. https://doi.org/10.1016/S0079-6611(02)00024-1

Siedler, G., Griffies, S. M., Gould, J., & Church, J. A. (2013). *Ocean circulation and climate. A 21st century perspective*. Academic Press, Elsevier.

Stephenson, D., & Bryan, K. (1992). Large-scale electric and magnetic fields generated by the oceans. *Journal of Geophysical Research*, *97*(C10), 15467–15480. https://doi.org/10.1029/92JC01400

Tarantola, A. (2005). *Inverse problem theory and methods for model parameter estimation*. SIAM.

Trossman, D. S., Tyler, R. H., & Pillar, H. R. (2024). Physical oceanographic factors controlling the ocean circulation-induced magnetic field. *Phil. Trans. R. Soc. A.*, *382*(2286), 20240076. https://doi.org/10.1098/rsta.2024.0076

Tyler, R. H., Maus, S., & Lühr, H. (2003). Satellite observations of magnetic fields due to ocean tidal flow. *Science*, *299*(5604), 239–241. https://doi.org/10.1126/science.1078074

Tyler, R. H., & Mysak, L. A. (1995). Motionally-induced electromagnetic fields generated by idealized ocean currents. *Geophysical and Astrophysical Fluid Dynamics*, *80*(3–4), 167–204. https://doi.org/10.1080/03091929508228954

Tyler, R. H., Mysak, L. A., Oberhuber, M., & Josef (1997). Electromagnetic fields generated by a three dimensional global ocean circulation. *Journal of Geophysical Research*, *102*(C3), 5531–5551. https://doi.org/10.1029/96JC03545

Velímský, J. (2025). Chapter two - Electromagnetic induction in the Earth's mantle and oceans: A spherical-harmonic approach. In C. Schmelzbach, A. Mittelholz, N. Schnepf, & S. Kang (Eds.), *Electromagnetic methods: Theory and applications* (Vol. 66, pp. 23–67). Elsevier. https://doi.org/10.1016/bs.agph.2025.06.004

Velímský, J., Šachl, L., & Martinec, Z. (2019). The global toroidal magnetic field generated in the Earth's oceans. *Earth and Planetary Science Letters*, *509*, 47–54. https://doi.org/10.1016/j.epsl.2018.12.026

Williams, R. G., & Follows, M. J. (2011). *Ocean dynamics and the carbon cycle*. Cambridge University Press.

Winch, D. E., & Runcorn, S. K. (1993). Geomagnetic observatory data and ocean circulation. *Exploration Geophysics*, *24*(2), 139–144. https://doi.org/10.1071/eg993139

Yamazaki, Y., & Maute, A. (2016). Sq and EEJ—A review on the daily variation of the geomagnetic field caused by ionospheric dynamo currents. *Space Science Reviews*, *206*(1–4), 299–405. https://doi.org/10.1007/s11214-016-0282-z

Zhang, K. (2023). A novel geomagnetic satellite constellation: Science and applications. *Earth and Planetary Physics*, *7*(1), 4–21. https://doi.org/10.26464/epp2023019

21699291, 2026, 11, Downloaded from https://agupubs.onlinelibrary.wiley.com/doi/10.1029/2026JC024496 by Christopher Finlay - Danish Technical Knowledge , Wiley Online Library on [12/11/2026]. See the Terms and Conditions (https://onlinelibrary.wiley.com/terms-and-conditions) on Wiley Online Library for rules of use; OA articles are governed by the applicable Creative Commons License